https://doi.org/10.5194/egusphere-2026-5633
Preprint. Discussion started: 11 November 2026
© Author(s) 2026. CC BY 4.0 License.

Geophysically-informed modelling and interpretation of cosmic-ray neutron sensing response to soil moisture spatiotemporal dynamics

Luca Peruzzo[1,*], Viola Cioffi[1], Mirko Pavoni[1], Markus Köhli[2], Jannis Weimar[2], Matteo Censini[1], Daniele Penna[3,4], Francesca Manca di Villahermosa[3], Paolo Benettin[5], and Giorgio Cassiani[1]

[1] Department of Geosciences, University of Padova, Padova, Italy
[2] Department of Physics, Heidelberg University, Heidelberg, Germany
[3] Department of Agriculture, Food, Environment and Forestry, University of Firenze, Italy
[4] Department of Forest Engineering, Resources and Management , Oregon State University, Corvallis, OR, USA
[5] Institute of Earth Surface Dynamics, University of Lausanne, Lausanne, Switzerland
[*] Corresponding author: luca.peruzzo.1@unipd.it

Abstract

Soil moisture and its dynamics have direct hydrological and ecological impacts, from the local field scale to the regional and global scales. Working on a gently-sloping vineyard with grassed interrows, this study combines soil moisture monitoring from cosmic-ray neutron sensing (CRNS) and soil sensors, geophysical characterizations, and CRNS numerical simulations. Multi-scale electrical resistivity tomography and frequency-domain electromagnetic mapping highlight a fingering transition from a clayey substrate to a fractured-karstic marl, both overlain by a more worked and homogeneous soil. Together with ancillary weather data, this spatial information and the associated infiltration dynamics explain how CRNS and nearby soil sensors respond differently to precipitation, depending on season, soil conditions, and rainfall characteristics. This highlights the critical interplay between spatiotemporal soil moisture dynamics and CRNS signal nonlinearity and nonuniqueness. CRNS numerical modelling further investigates this interplay, specifically in terms of lateral dominance of drier regions and amplified sensitivity to moisture changes at the soil surface, here induced by light rainfall events. A theoretical generalization of the dry-dominance is provided, based on Jensen's inequality and a third-order Taylor expansion of the CRNS response function. Together, field observations and numerical modelling inform a conceptual soil hydrology model that describes the observed soil moisture spatiotemporal dynamics. The results reinforce the value of more spatially informed, hydrology-based CRNS applications, a key step toward capitalizing on recent CRNS methodological advances and achieving a better integration with soil moisture networks and multi-methodological hydrological observatories.

1 Introduction

Soil moisture and its dynamics have direct hydrological and ecological impacts, from the local field scale to the regional and global scales (Vereecken et al., 2008, 2022). Soil moisture sensors have been the most common and direct solution to monitor soil moisture, and they remain the industry standard (Shafi et al., 2019; Yu et al., 2021). Nonetheless, soil sensors have well known methodological weaknesses and conceptual limitations. Above

https://doi.org/10.5194/egusphere-2026-5633
Preprint. Discussion started: 11 November 2026
© Author(s) 2026. CC BY 4.0 License.

all, they are very sensitive to installation factors and only provide localized information (Evett et al., 2008). This contrasts with the increasing understanding and interest in soil moisture spatiotemporal variability over the relevant spatial scales, from field to regional to global (Babaeian et al., 2019; Beven, 2008). While their point-scale nature is self-evident, their interpretation necessarily relies on assumptions regarding the spatiotemporal soil properties and water dynamics (Beven, 2008; Binley et al., 2015). These assumptions are often implicit and remain rarely supported by additional information or sufficient statistical analyses, because of practical and economical constraints (Vereecken et al., 2016; Baatz et al., 2017).

Cosmic-ray neutron sensing (CRNS) is an emerging technology that fills the above technological gap and need for moisture measurement at the relevant field scale (Zreda et al., 2008; Desilets et al., 2010). With a detector conveniently located above the ground, CRNS integrates the soil moisture information over a footprint with a radius of 100 - 250 m and a soil depth of a few tens of centimeters (Rasche et al., 2021; Köhli et al., 2015). The actual sensitivity distribution is a complex function of above- and below-ground variables and properties, including soil water content itself, soil density, other hydrogen sources, and air humidity (Köhli et al., 2021; Ruehlmann and Körschens, 2009). Köhli (2026) reviewed numerous studies that addressed these and other fundamental aspects. The advances led to more accurate theoretical and numerical models regarding the relationship between volumetric water content (VWC) and CRNS intensity.

An important property of this relationship is its nonlinearity, as the function flattens towards high VWC. This implies that the CRNS intensity change, for a given VWC change, is inversely proportional to the VWC. This has been observed, numerically investigated, and understood (Zreda et al., 2008; Köhli et al., 2021). Nonetheless, it contrasts with the appealing concept of effective spatial averaging. In the presence of spatiotemporal VWC dynamics, the nonlinearity implies that VWC changes in drier regions have a stronger impact on the CRNS signals, hereinafter dry-dominance. A few studies explored the main possibilities for more spatially-aware CRNS, including roving (Baatz et al., 2017; Schrön et al., 2018; Zhang et al., 2024), network solutions (Franz et al., 2015; Brogi et al., 2026; Heistermann et al., 2023) at the watershed or field scale, and directional shielding (Francke et al., 2022). The same authors discussed, however, how the "field of view of the probe is diluted" by the neutron scattering itself. This, combined with common count rates, has slowed the methodological advances in this sense (Jakobi et al., 2020; Francke et al., 2022). A second aspect is the high, but also variable, CRNS sensitivity to changes at the soil surface, e.g., light rain and shallow ET dynamics (Franz et al., 2012; Scheiffele et al., 2020). Recent studies investigated and highlighted the importance of visually apparent surface features associated with drier regions, such as dry roads in agricultural environments (Schrön et al., 2018) and snow-free patches in otherwise snow-covered areas (Schattan et al., 2019). While the above aspects have been observed and numerically investigated, the associated nonlinearity and nonuniqueness of the CRNS response have been less studied, particularly regarding their interplay with subsurface soil heterogeneity and complex soil hydrology scenarios.

Geophysical methods have been used to characterize the subsurface properties and heterogeneity (Rubin and Hubbard, 2005; Vereecken et al., 2006). Among geophysical methods, electrical resistivity tomography (ERT) and frequency-domain electromagnetic mapping (FDEM) have been commonly used in hydrological, ecological, and agricultural applications (Binley et al., 2015; Atekwana and Slater, 2009; Garré et al., 2021). Both ERT and FDEM measure the electrical conductivity, or resistivity, of the subsurface, interpreted

https://doi.org/10.5194/egusphere-2026-5633
Preprint. Discussion started: 11 November 2026
© Author(s) 2026. CC BY 4.0 License.

as a proxy for water content, water chemistry, and relevant soil properties. FDEM uses pairs of solenoids to induce and measure an electromagnetic response of the subsurface and provide convenient mapping (Boaga, 2017; Von Hebel et al., 2021; O'Leary et al., 2024). Possibly guided by the FDEM mapping, ERT can further characterize or monitor specific areas thanks to its spatial flexibility (Uhlemann et al., 2024; Peruzzo et al., 2024; Mary et al., 2018) and control over the data quality (Tso et al., 2017; Binley and Daily, 1995). The gained insight can, in turn, enhance and validate the interpretation of the FDEM maps (Wang et al., 2015; Peruzzo et al., 2025; Carrera et al., 2024). While ERT and FDEM have been increasingly used in this sense, their capability to provide direct and quantitative VWC information remains limited, hindered by the complexity of the petrophysical relationships and site variability (Glover, 2017). Rare exceptions took advantage of ERT monitoring to constrain the resistivity - VWC relationship through hydrological models, i.e., hydrogeophysical modelling (Binley et al., 2015; Rossi et al., 2015). Alternatively, they relied on laboratory sample calibrations or soil sensors measuring both VWC and electrical resistivity (Brunet et al., 2010; Pini et al., 2026). This, however, necessarily reintroduces the concerns regarding the spatial heterogeneity and consequent representativeness of the samples, as well as non-trivial and time-consuming laboratory work. Hence, an integration with more VWC-specific and monitoring methodologies remains desirable (Hubbard et al., 2018; Boyd et al., 2024).

As introduced, soil sensors and CRNS have distinct advantages and disadvantages, and they can potentially complement each other to offer what may be considered the present and near-future standard for VWC monitoring. This study combines VWC monitoring with soil sensors and CRNS, field geophysical characterizations, and CRNS numerical simulations. This study aims to 1) investigate the interplay of natural, complex soil hydrological dynamics and CRNS nonlinearity and nonuniqueness, 2) provide a suitable geophysical characterization of the subsurface lateral and vertical variability to guide the CRNS analysis, 3) investigate such hydrological variability and dynamics with CRNS numerical simulations, validating and generalizing the CRNS results, 4) combine the geophysical spatial information, VWC temporal information from CRNS and soil sensors, and the gained insight on the CRNS sensitivity to define a soil hydrological model, and 5) provide a theoretical generalization of the dry-dominance.

2 Materials and Methods

The study site is located in Borgo Grignanello, Tuscany, central Italy, in the Chianti wine region of the Apennines (43°31'18.4"N, 11°17'04.6"E, WGS84). The land use is dominated by vineyards and olive groves, and approximately 60 % of the territory is classified as forest (Masnaghetti, 2022). The area is hilly, with elevations ranging from 300 to 500 m above sea level, and highest sectors reaching up to 900 m. The study site is a one-hectare vineyard located on gentle and north-facing slope, with steepness lower than 5 %. Geologically, the study site lies on the grey and brown argillite of the Sillano–Santa Fiora Formation, but with a transition to the marls and marly limestones of the Monte Morello Formation just south - uphill of the vineyard (Carmignani et al., 2013). The resulting soil has a fine texture and variable depth above marly levels, whose presence is also confirmed by nearby outcrops.

The grape vines are mainly the local Sangiovese and Canaiolo varieties. The plants were planted in 1977 with a low density of 3000 plants per hectare, against the 6000 plants per hectare of more typical modern vineyards. The interrows are managed with shallow

https://doi.org/10.5194/egusphere-2026-5633
Preprint. Discussion started: 11 November 2026
© Author(s) 2026. CC BY 4.0 License.



Figure 1: Map of the Grignanello field site showing the geophysical survey areas and the locations of the CRNS probe, soil samples, and soil moisture sensors. Map source: Google Maps, imagery ©2026 Airbus, Maxar Technologies.

https://doi.org/10.5194/egusphere-2026-5633
Preprint. Discussion started: 11 November 2026
© Author(s) 2026. CC BY 4.0 License.

mechanical weeding alternatively applied to adjacent rows to maintain a thin sward. No irrigation is applied, in line with Chianti regulations. Climate in the area is Mediterranean, with an average of 800 mm of rainfall per year, typically concentrated in autumn and spring. The average temperature ranges from 5 °C in winter to about 25 °C in summer, with respective daily temperature excursions of about 8 and 15 °C.

Figure 1 shows the vineyard plot with its immediate surroundings and the positioning of soil sensors, CRNS sensor, soil samples, and geophysical measurements. A pair of 5TM sensors by Meter Group for VWC and temperature was installed in 2022 at 10, 25, 50, 75, and 100 cm depth. The shallowest installation at 10 cm represents a compromise between sensitivity to shallow water dynamics and a reliable installation, also compatible with the mechanical weeding. A datalogger CR1000 by Campbell Scientific recorded the VWC data with a logging period of 5 minutes. An ATMOS41 weather station with pluviometer by Meter Group and an additional Davis pluviometer by Solem were installed on site a few meters from soil sensors. Additional precipitation data from a nearby pluviometer of the regional network located in Barberino Tavarnelle, 4 km from site, supported the site data. A StX S2+ neutron detector by StyX Neutronica was installed in May 2024 about 20 m north of the soil sensors. This position was chosen as a compromise between the proximity to the soil sensors and a more central position within the vineyard plot, deemed important for the detector footprint.

2.1 Soil samples

Twenty-six samples were collected for the calibration of the CRNS response on November 15 2024, between 11 am and 2 pm (Fig. 1). The samples were collected with a closed-face bucket auger with a diameter of 12.5 cm and a length of 40 cm. The samples were collected at 13 locations radially distributed in four opposite directions relative to the cosmic-ray sensor, at the distances of 0, 5, 20, and 50 m (Schrön et al., 2017). At each position, two samples were collected, the first one from 0 to 15 cm depth and the second from 15 to 30 cm. The samples were directly moved from the sampler into zip plastic bags, which were then sealed to avoid water loss. The wet weight of the samples was measured in the field right after sealing the sample bags.

The samples were analyzed for water content, soil bulk density, texture, and organic content. The soil density was estimated after drying the samples at 55 °C for two weeks, i.e., a few days after reaching constant weight. The water content was calculated from the weight loss. The bulk soil density was calculated from the dry weight and known geometry of the closed-face bucket auger. The organic matter content was estimated with the loss-of-ignition method. Two sub-samples of 5 g were taken from each sample and heated to 500 °C for 4 h (Heiri et al., 2001). Temperature and duration were chosen to maximize the loss of the organic matter while also limiting the concurrent loss of carbonates (Li et al., 2017) and clay structural water (Howard and Howard, 1990). Nonetheless, some loss of structural water is expected and thus the correction suggested by Hoogsteen et al. (2015) was applied, based on the clay content from the soil samples and with the recommended factor of 0.075 kg kg^{-1}. In contrast, the overestimation caused by the difference between initial oven drying at 55 °C and 105 °C has been shown to be a smaller factor, <1 % for the local soil type (O'Kelly, 2005). Heidbüchel et al. (2016) discussed and included these possible sources of errors with regard to the CRNS calibration. For the soil texture, the fine earth fraction (smaller than 2 mm) was obtained by drying, crushing and sieving part of the samples. The fine earth fraction was then analyzed with a Mastersizer by Malvern Panalytical (Callesen et al., 2018).

https://doi.org/10.5194/egusphere-2026-5633
Preprint. Discussion started: 11 November 2026
© Author(s) 2026. CC BY 4.0 License.

2.2 CRNS

A StX S2+ detector by StyX Neutronica was used (Ney et al., 2021). The detector consists of three 125-cm tubes that use a copper foil with sputter deposited $^{10}B_4C$ as converter, and Ar – CO_2 as counting gas (Weimar et al., 2020; Heistermann et al., 2023; Köhli and Weimar, 2026). The detector casing has length of 146 cm and diameter of 28 cm, and it consists of a 25 mm high-density polyethylene moderator and a gadolinium shield for thermal neutrons (Brogi et al., 2023; Köhli et al., 2018). The CRNS monitoring started on November 14 2024 and lasted until October 21 2025. The detector recorded 15-min averages of count per minute. Raw count-per-hour data were considered outliers and dropped outside the range 1200 - 2500, based on detector characteristics and initial field tests. The data were then further averaged into 4-hour data points for the VWC analysis. The CoRNy toolbox for Python was used to filter, process, calibrate and convert the CRNS data into VWC (Schrön et al., 2025; Van Rossum and Drake, 2009). CoRNy was configured to use the Universal Transport Solution as conversion function (Köhli et al., 2021).

$$N(\theta, h) = N_D \left(\frac{p_1 \quad p_2\theta}{p_1 \quad \theta} \left(p_0 \quad p_6 h \quad p_7 h^2 \right) \quad e^{-p_3\theta} \left(p_4 \quad p_5 h \right) \right) \tag{1}$$

Where θ is the gravimetric or volumetric water content and $N(\theta, h)$ is the above-ground neutron flux measured by the CRNS, as a function of the absolute air humidity h ($g\,m^{-3}$) and water content (Köhli, 2026). The eight parameters p_i were determined in previous numerical investigations (Köhli et al., 2021). The scaling constant N_D was calibrated based on the average water content from the soil samples and absolute air humidity at the sampling time (Köhli et al., 2021; Schrön et al., 2017; Heidbüchel et al., 2016). After the conversion, the data were smoothed using a Savitzky-Golay filter of third order over six 4-hour periods (Savitzky and Golay, 1964).

Soil bulk density, clay content, and organic matter content from the samples were used for the correction of the neutron count time series measured by the CRNS. The correction for the organic matter was calculated by multiplying its gravimetric content by 0.556, which gives the water content with equivalent hydrogen contribution for a cellulose composition (Franz et al., 2015; Nelson and Sommers, 1982). The correction for lattice water was obtained by multiplying the clay fraction by 0.18 (Franz et al., 2012; Greacen, 1981). The soil bulk density was used in CoRNy to define the model soil density for the simulation of the neutron interactions and pathways (Tian et al., 2016; Desilets et al., 2010). The correction for the incoming radiation was based on Schrön et al. (2015) with data from the Jungfraujoch (CH) neutron monitor station. The air pressure correction was based on Zreda et al. (2012), with mass attenuation length of 136 $g\,cm^{-2}$.

2.3 Electrical and Electromagnetic surveys

Electrical resistivity tomography (ERT) and frequency-domain electromagnetic induction (FDEM) surveys were performed to characterize the spatial heterogeneity of the site subsurface. A total of eight ERT 2D sections were acquired with a Syscal Terra resistivity meter by Iris. Four ERT lines were acquired with an electrode spacing of 1 m on November 14 2024, three with 72 electrodes longitudinally to the plant lines and one with 48 electrodes orthogonal to the plant and crossing longitudinal lines. Four shorter and higher resolution lines were acquired on March 25 2025. These lines were positioned on two specific positions along the longer longitudinal ERT lines, based on their results and FDEM maps. On each

https://doi.org/10.5194/egusphere-2026-5633
Preprint. Discussion started: 11 November 2026
© Author(s) 2026. CC BY 4.0 License.

position, two lines were acquired using 72 electrodes with an electrode spacing of 40 and 20 cm, the short 20-cm one being centered along the longer one to overlap their sensitivities. A mixed sequence of 5474 measurements with dipole-dipole skips 3 and 6, and gradient configurations was used. The sequences included full reciprocals, which were used to estimate the measurement error and filter the dataset (Binley and Daily, 1995; Tso et al., 2017). Processing and inversion were carried out with ResIPy (Blanchy et al., 2020) and visualized in ParaView (Ahrens et al., 2005).

FDEM mapping was carried out over the vineyard plot using a CMD Mini Explorer on April 4 2024 and November 14 2024, Fig. 1. The Mini Explorer has an operating frequency of 30 kHz and three receiving coils with separations of 0.32, 0.71, and 1.18 m. These characteristics give a shallow investigation with maximum sensitivity and resolution in the top 1 m (Bonsall et al., 2013; Carrera et al., 2024; McNeill, 1980). The surveys were carried out in horizontal coplanar modes, with the instrument at a height of 10 cm and a sampling interval of 1 s. The survey covered every other plant interrow, walking along its center to maximize the distance from the metallic plant supports. This distance was deemed sufficient considering the interrow width of 2.8 m, the relatively small footprint of the Mini Explorer, and its longitudinal direction (Guillemoteau and Tronicke, 2015). The data were first corrected with EMagPy to remove the manufacturer calibration factors and to numerically recalculate the apparent conductivities. The data were then calibrated using the ERT sections with 20-cm electrode spacing to take advantage of their high resolution in the FDEM investigation depth. Although relatively short, the 20-cm ERT sections were located in the conductive and resistive regions and thus suitably spanned the resistivity range for the FDEM calibration. Finally, the data were inverted using the cumulative sensitivity forward model and the default L-BFGS-B optimization algorithm (McLachlan et al., 2021; Byrd et al., 1995). The data were interpolated and visualized in QGIS with the inverse-distance-weighted method (Dawson et al., 2026).

2.4 CRNS numerical modelling

Monte Carlo simulations of neutron transport were performed with URANOS (Ultra Rapid Neutron-Only Simulation) to investigate the CRNS response to field-based scenarios and the associated footprint characteristics (Schrön et al., 2017; Brogi et al., 2023; Rasche et al., 2021). URANOS simulates the neutron transport from a source layer with statistical distribution of neutron energy and incoming angles (Sato and Niita, 2006; Sato, 2015, 2016), positioned high above the ground. The neutrons are then tracked in the thermal and epithermal regime through elastic collisions, inelastic collisions, and neutron emission processes, till their detection and absorption (Köhli et al., 2023). The model domain was defined as a square with a side of 700 m. The neutron source was defined as a square with a side length of 1000 m and a thickness of 30 m, positioned between 50 and 80 m above ground. Each simulation generated and tracked 5×10^8 neutrons. A transparent virtual cylindrical detector with a radius of 3 m and height of 1.5 m was positioned 1 m above ground level at the center of the model. Multiple detections of the same neutron and detections of neutrons that had no previous interaction with the soil were ignored. The simulated CRNS counts were then converted back to VWC using CoRNy, as for the field data.

Two initial sets of tests, dry and wet, with homogeneous models were performed to test the correctness of the forward simulation (VWC to count) and back conversion from count to VWC (Tab. 1). After the tests, two sets of VWC scenarios investigated the associated CRNS signals and their difference with respect to the soil sensors (Tab. 1). The first set

https://doi.org/10.5194/egusphere-2026-5633
Preprint. Discussion started: 11 November 2026
© Author(s) 2026. CC BY 4.0 License.



explored the dry dominance deriving from the nonlinear relationship between VWC and CRNS intensity (Zreda et al., 2008; Köhli et al., 2021). A two-region model was based on the geophysical characterization, measured VWC time series, and geological information (Fig. 2). The different VWC and soil bulk densities were assigned to the two regions, simulating four time steps along two different drying curves. The VWC was set to 25, 15, 10, and 5 % for a dry - permeable region, representing a fractured-karstic marl (marly region). The corresponding VWC values of the wet - less permeable region were set to 40, 35, 32.5, and 30 %, representing the VWC dynamics in a clayey fine-textured substrate, attributable to the argillite (clayey region). The CRNS was positioned in the dry region and about 15 m from the transition of the two regions, as in field setup. The simulations were then repeated inverting the dry and wet regions, i.e., with the detector in the wet region. Finally, a third and more general test of dry dominance was designed by replacing the geophysics-based boundary outline with a straight line and positioning the detector right above it, rather than 15 m inside the dry region. These second and third geometries aimed to explore the dry-dominance and geometrical contributions observed in the first, field-based scenario and field data.

The second set explored the high sensitivity of the CRNS to light precipitation events, based on the recorded time series of CRNS VWC and precipitation at the site. A homogeneous model with fixed porosity and VWC water content was used, while the effect of a light rain was explored with three scenarios (Tab. 1). In the first, a 7-mm layer of water was positioned above the soil to simulate the water held by the grass or hydrophobic - dry soil. In the second, the 7 mm were distributed in the topsoil, saturating the first 1.4 cm, reaching a VWC of 50 %. In the third, the 7 mm were distributed over the top 2.8 cm, reaching a VWC of 25 %.

Table 1: Description of the 23 scenarios simulated with URANOS. Within each set, the simulations differ according to the simulated scenarios and VWC values associated to the scenario regions. In first set, the vertical lines represent the presence of two regions with different VWC values, which progressively increase on both sides.

Scenarios	Porosity %		VWC %	
Initial tests				
Homogeneous dry	30		5, 10, 15, 20, 25	
Homogeneous wet	50		20, 30, 32.5, 35, 40	
I Set, dry dominance				
Symmetric	30	50	5, 10, 15, 25	30, 32.5, 35, 40
Field, detector in the dry region	30	50	5, 10, 15, 25	30, 32.5, 35, 40
Field reversed	50	30	30, 32.5, 35, 40	5, 10, 15, 25
II Set, thin top water layer				
Homogeneous, no top water	50		15	
14 mm topsoil layer at 50 % VWC	50		15	
28 mm topsoil layer at 25 % VWC	50		15	

The URANOS simulations return a count of detected neutrons for each scenario of soil density and VWC. The additional dependence on the total number of simulated neutrons was removed by converting the count into count rate (count per second). The conversion factor was derived by matching the simulated counts to the field count rates when both field and simulation model have a VWC of 20 %. This ensured the comparability of the simulations with one another and with the field values, but also allowed the successive conversion from count rate to VWC using the UTS model in CoRNy. The N_D for the UTS

https://doi.org/10.5194/egusphere-2026-5633
Preprint. Discussion started: 11 November 2026
© Author(s) 2026. CC BY 4.0 License.

function was calibrated with the tests datasets, as their homogeneous conditions of soil density and VWC provide an unambiguous target for the calibration. Two N_D values were estimated by minimizing the misfit between the VWC inputs in URANOS and UTS inverted VWC, considering the five VWC values in each of the two homogeneous scenarios. This is equivalent to the N_D calibration for the field data, described above, with the known URANOS VWC values serving as "ideal" field samples. The two N_D were used for the conversion of the homogeneous tests, while their average was used for the successive scenarios in sets I and II.

3 Results

3.1 FDEM and ERT

The FDEM surveys collected 4216 measurements in April and 1746 in November 2024. The data quality was generally good, the ERT-based calibration had R^2 of 0.96, 0.94 and 0.89, and the inversion misfits were 4, 5, and 2 % (root mean square percentage error), respectively for the 0.32, 0.71, and 1.18 m coil separations. Figure 2 shows a shallow (25 cm) and a deep (1 m) slice from the inverted FDEM model obtained on April 12 2024. The two slices highlight the difference between shallow and deep spatial heterogeneity. The deep slice shows the presence of an irregular, fingering transition to a more resistive subsurface to the west, with the apparent resistivity increasing from 15 to about 45 Ω m. In particular, a more conductive intrusion (<20 Ω m) reaches and surrounds the region of the soil sensors, while the CRNS detector remains on the more resistive domain, about 12 m north. In contrast, the shallow slice is more homogeneous, the intrusions are still visible and have similar resistivity values (15 Ω m) but there is no clear transition to the more resistive domain.

The eight ERT datasets, 5474 measurements each, had high data quality and were filtered with a 2 % reciprocal threshold, which removed between 0.0 and 0.4 % of the measurements. The same 2 % error was also used for the ERT inversions. Figure 3 shows the four 2D ERT sections acquired with an electrode spacing of 1 m, while Fig. 4 shows the successive high-resolution sections (0.4 and 0.2 m electrode spacing). The large-scale sections captured the presence and geometry of the conductive intrusion, which reaches and surrounds the soil sensors. The conductive intrusion interests the uphill - south part of the three longitudinal sections. In section L1, the conductive intrusion surfaces for the entire first part of the section, where it remains shallow and rests on top of a well visible resistive substrate. This substrate becomes shallower and surfaces around meter 35 of the section, thus confining the conductive body. In section L2, the surface exposure shrinks as the conductive body becomes deeper and covered by a shallower resistive layer to the south. The conductive layer remains well visible below this shallower layer and then surfaces between meters 15 and 30. In section L3, this shrinking and covering further progresses, the conductive body remains covered until meter 25, from where it surfaces for only about 5 m. The transversal section T confirms the continuity of this conductive intrusion across the longitudinal sections, showing fairly constant resistivity values (15 Ω m) and depth of about 3 m. A particularly conductive region (10 Ω m) between meters 2 and 6, and covered by the thin resistive layer well matches the L3 profile at the section crossing.

The high-resolution sections in Fig. 4 confirm the differences between the conductive region associated with the intrusion (c, d) and the surrounding resistive region (a, b). In addition, they also capture the presence of a shallow layer attributable to a more homogeneous -

https://doi.org/10.5194/egusphere-2026-5633
Preprint. Discussion started: 11 November 2026
© Author(s) 2026. CC BY 4.0 License.

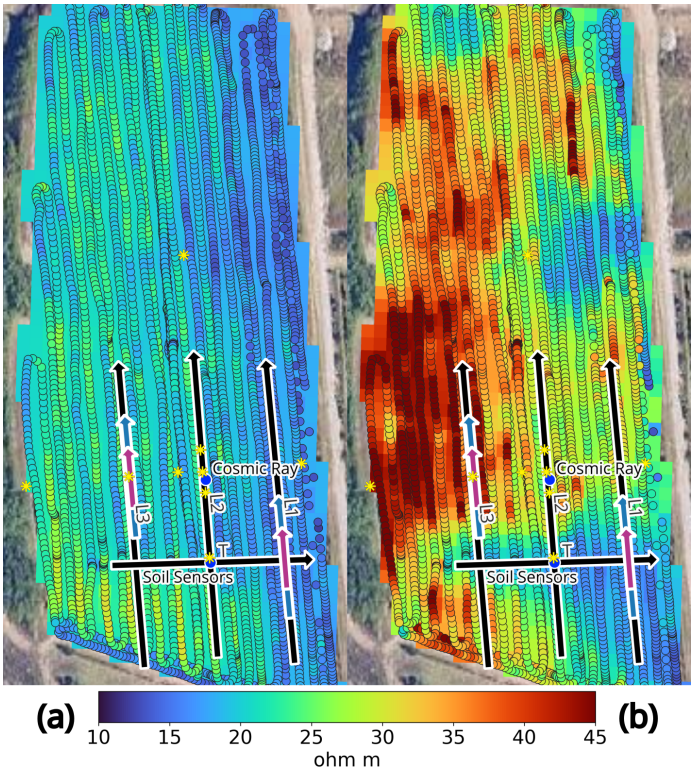


Figure 2: Shallow (a, 25 cm) and deep (b, 1 m) slices of the FDEM inverted model. The deep slice reveals irregular, fingering transition to a more resistive subsurface to the west, while the shallow slice remains less resistive and is thus more homogeneous. The markers show the individual data points over their inverted and interpolated model (inverse distance weighted interpolation function in QGIS). ERT lines (arrows), soil sensors, CRNS probe, and soil sampling locations are also shown for spatial reference (Fig. 1). Background map source: Google Maps, imagery ©2026 Airbus, Maxar Technologies.

https://doi.org/10.5194/egusphere-2026-5633
Preprint. Discussion started: 11 November 2026
© Author(s) 2026. CC BY 4.0 License.

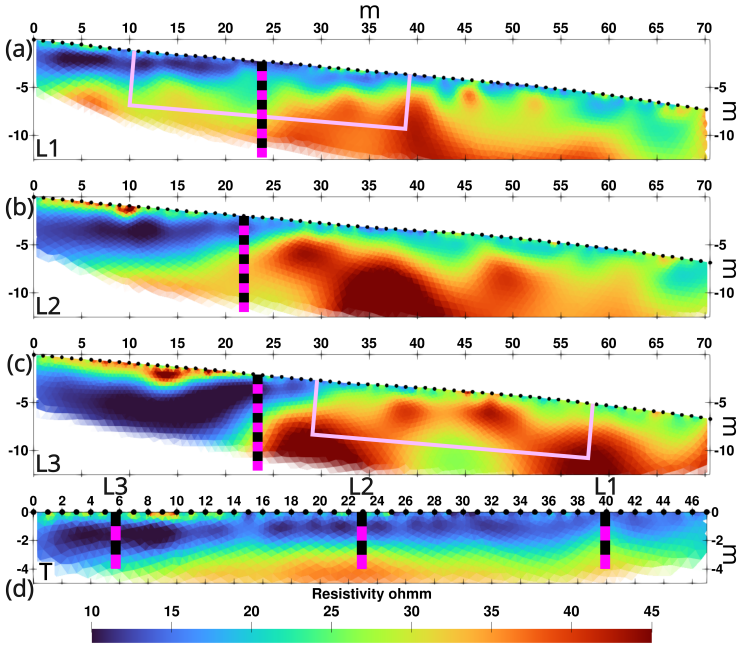


Figure 3: ERT inverted sections from the arrays with an electrode spacing of 1 m. As in Fig. 1, (a), (b), and (c) are the longitudinal lines with 72 electrodes, L1, L2, and L3, respectively. (d) shows the transversal T line, with 48 electrodes. The purple-black vertical markers indicate the crossing position of the transversal section along the longitudinal ones (a, b, c), and vice versa (d). The purple-black alternation is scaled to indicate 1 m depth intervals. The pink rectangles indicate the positions of the 40-cm ERT sections (Fig. 4).

https://doi.org/10.5194/egusphere-2026-5633
Preprint. Discussion started: 11 November 2026
© Author(s) 2026. CC BY 4.0 License.

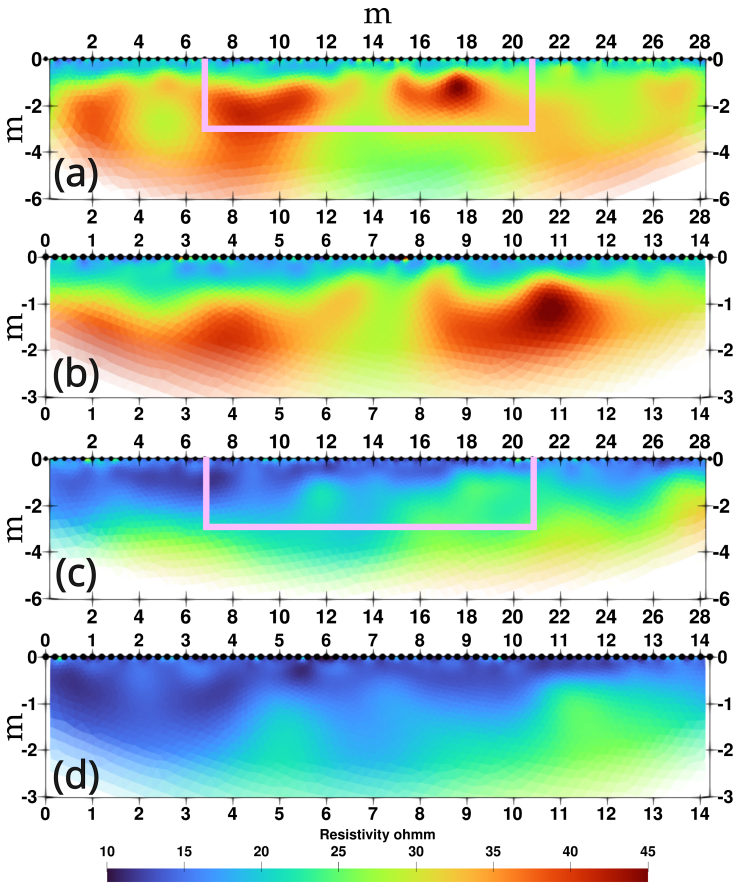


Figure 4: ERT inverted sections from the arrays with an electrode spacing of 40 cm (a and c) and 20 cm (b and d). (a) and (b) show the sections acquired along L3 (western and more resistive region), and (c) and (d) the ones along L1 (eastern and less resistive region), Figs. 2 and 3. The pink rectangles indicate the position of the short ERT sections (20-cm electrode spacing) along the longer sections (40-cm electrode spacing).

https://doi.org/10.5194/egusphere-2026-5633
Preprint. Discussion started: 11 November 2026
© Author(s) 2026. CC BY 4.0 License.

worked soil, which was not resolved by the 1-m spacing sections. In the high-resolution sections along L3 (a, b), the soil layer has a thickness of about 25 cm and covers the entire section, extending beyond the transition point captured by L3. This soil layer is here resolved with values of about 20 Ω m, while it appears mixed and smoothed with the underlying resistive domain in the 1-m section L3. Finally, the high-resolution section also better resolves the spatial heterogeneity below this soil layer, for example the two resistive anomalies in Fig. 4b and the particularly thick and conductive region at the beginning of Fig. 4d. This subsurface heterogeneity and the relatively homogeneous soil layer on top support the FDEM inverted model: the soil layer would control the shallow model slice, and the heterogeneity underneath the deep model slice.

3.2 Soil samples

All the twenty-six shallow soil samples were fully augered to the expected depth of 15 cm. In contrast, the collection of the deep samples (15 to 30 cm depth) was locally hindered by the rocky - marl substrate, which limited the manual augering depth. This occurred near and west of the CRNS detector, i.e., in the resistive domain identified by the FDEM and ERT surveys. The average bulk density was $1.28 \pm 0.29\,\mathrm{g\,cm^{-3}}$, with an average $1.18\,\mathrm{g\,cm^{-3}}$ for the shallow and $1.38\,\mathrm{g\,cm^{-3}}$ for the deep samples. These bulk density values agree with literature values on vineyards and grassland (Panagos et al., 2024), also considering the soil organic matter and clay contents (Robinson et al., 2025; Ruehlmann and Körschens, 2009), and the limited - light use of agricultural machinery (Van Dijck and Van Asch, 2002; Raper, 2005). The average VWC was 29.0 ± 6.4 %, with an average 27.5 % for the shallow and 30.5 % for the deep samples. The spatial distribution of VWC and density did not present significant spatial patterns, the main exception being the two lowest VWC values 20.4 % on the westernmost and shallow samples. The textural analysis of the samples yielded a silt loam texture with and average 19 % of clay and 74 % of silt, with no significant spatial pattern. The loss-of-ignition analysis resulted in an average soil organic matter of 6 ± 1 %, in good agreement with literature values for comparable soil textures and vegetation conditions (Guillaume et al., 2021; Loveland, 2003; Lugato et al., 2021).

3.3 Volumetric water content

The CRNS monitoring provided 2046 4-hour data points, with associated data of temperature, humidity, and pressure for the CRNS corrections. The average soil bulk density of $1.28\,\mathrm{g\,cm^{-3}}$ was used in CoRNy. Similarly, the average VWC of 29 % was used to calibrate the scaling constant N_D of the universal transport solution (Eq. 1). The corrections for clay lattice water and soil organic matter resulted in a 3.4 % and 3 % of water equivalents, respectively. The average depth of the footprint calculated by CoRNy was 21 ± 4 cm, with a maximum depth of 35 cm in summer.

Figures 5, 6, and 7 show VWC time series from the CRNS and the shallow soil sensors, supported by precipitation, humidity, and temperature data. The CRNS and sensor VWC time series respond to the precipitations and seasonal changes, but also have significant differences. Figure 5 shows the time series over the winter period, in which the VWC from soil sensors remain homogeneous and stable with values about ≈45 %. In contrast, the CRNS time series shows stronger fluctuations, responding also to light precipitations. In addition, the VWC values range between 20 and 35 %, i.e., significantly lower than the soil sensors. Figure 6 shows a late-spring period when the soil dries in the absence of precipitation and with a temperature increase of 10 °C in less than a month. The CRNS

https://doi.org/10.5194/egusphere-2026-5633
Preprint. Discussion started: 11 November 2026
© Author(s) 2026. CC BY 4.0 License.

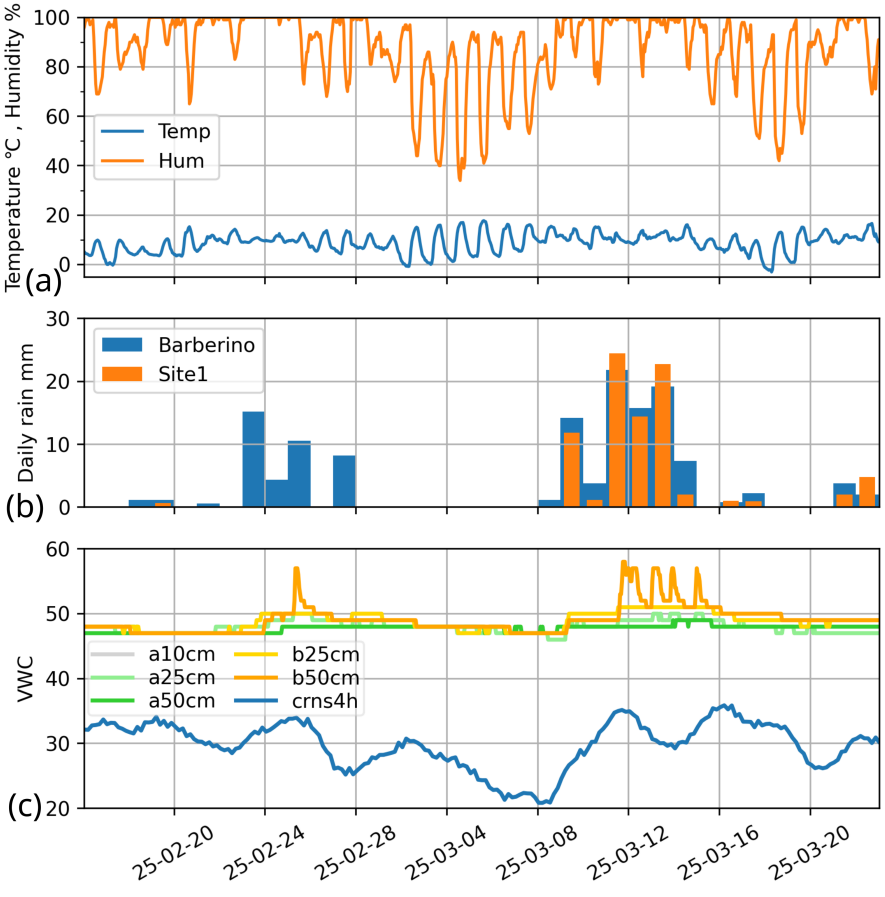


Figure 5: Time series in winter 2025. During this cold period, the soil sensor time series show higher and more stable VWC values compared to the CRNS estimates, with a limited response to precipitation inputs.

https://doi.org/10.5194/egusphere-2026-5633
Preprint. Discussion started: 11 November 2026
© Author(s) 2026. CC BY 4.0 License.

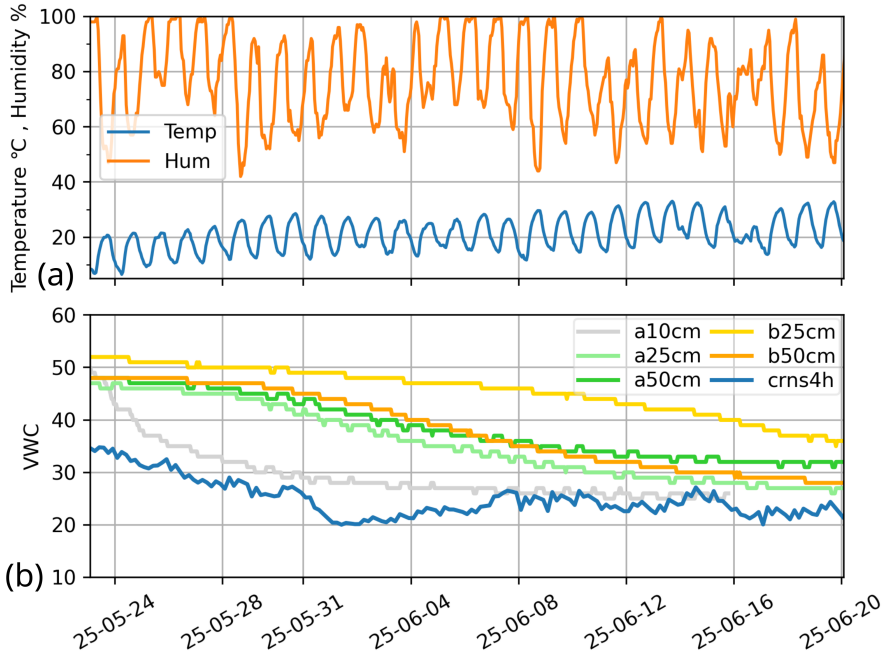


Figure 6: Time series in spring 2025. In this precipitation-free period, the VWC measured by the CRNS decreases earlier and more rapidly, while the soil sensors converge to similar VWC values as the temperatures increase.

https://doi.org/10.5194/egusphere-2026-5633
Preprint. Discussion started: 11 November 2026
© Author(s) 2026. CC BY 4.0 License.

series shows lower initial values reflecting the initial differences observed in winter and also faster than the sensor series, stabilizing by the first days of June, about two weeks before the soil sensors at 25 and 50 cm. In contrast, the soil sensor at 10 cm has a dry curve comparable to the CRNS series and also stabilizes by early June. Apart from these differences, the figure shows how all the time series tend to converge after a sufficiently long and hot period, indicating more homogeneous VWC field conditions.

Figure 7 shows the summer and fall periods, which presents a hot and dry period in early August and precipitation events of variable duration and intensity both before and after it. All the VWC series consistently respond to the more intense precipitation (>20 mm). However, the soil sensors are less consistent with regard to lighter precipitations. For example, the 10 mm of rain of July 13 are captured by the CRNS series but have no effect on the soil sensors, even though the sensors at 25 and 10 cm depth match the calculated depth of the footprint for this period (≈30 cm). Similarly, the soil sensors do not respond to the light rains that occurred in the second half of August, but only to the successive strong precipitation of August 29 (38 mm). This and two successive strong precipitations, although all different, also show how the drying-phase curves of soil sensors and CRNS change with decreasing temperatures and radiation. The soil sensor series flatten progressively. This is well visible for the 25-cm sensors because of their linear paths but the 10-cm seems affected too. As a consequence, the precipitation events and drying curve extend and start to overlap, giving an increasing VWC base line. In contrast, the steepness of the CRNS series remains similar over the three events, whose drying-phase curves remain distinct and return to VWC of about 20 % after each drying phase.

3.4 Numerical models

Figure 8 shows the results of the CRNS numerical simulations performed with URANOS and CoRNy to explore different scenarios of lateral and vertical VWC variability (Tab. 1). The initial dry and wet tests had homogeneous domains to evaluate the correct use of URANOS and CoRNy, and provide VWC references for the heterogeneous scenarios. The test results show a good agreement between the true VWC values (URANOS inputs) and the inverted VWC values obtained by converting the URANOS counts into VWC values with Corny. The simulated 5×10^8 neutrons ensured a minimum of 10 000 detections in all simulations, after excluding multiple and no-soil detections. Hence, the tests confirm the sufficient accuracy and statistical stability of the numerical procedure, assuming a Poisson distribution and thus a coefficient of variation of $n^{-1/2}$ (Zreda et al., 2012).

Figure 8a also shows the simulation results of the first set, exploring the CRNS sensitivity to lateral variation of VWC. The figure shows where the VWC values obtained from the three scenarios lie relative to the two reference dry and wet models. The Grignanello scenario used the two-domain simplification of the geophysics-based model (Fig. 8c), with the detector positioned within the dry region but near the boundary (red dot, Fig. 2). Hence, this simulation reproduced both the field geometry and expected VWC of the marly and clayey regions. The similarity between Dry and Grignanello results shows how the dry region dominates the overall behavior of this field-based model. The Reverse scenario maintained the same geometry and detector position, but it inverted the dry and wet domains so that the detector is in the wet domain. This set lies approximately half-way between the dry and wet tests, despite the detector now being 15 m inside the wet region, suggesting a balance between dry-dominance and detector proximity. The Symmetric scenario had a straight outline between the marly and clayey region, and the detector was positioned at the center, along the boundary, to isolate the dry-dominance from the

https://doi.org/10.5194/egusphere-2026-5633
Preprint. Discussion started: 11 November 2026
© Author(s) 2026. CC BY 4.0 License.

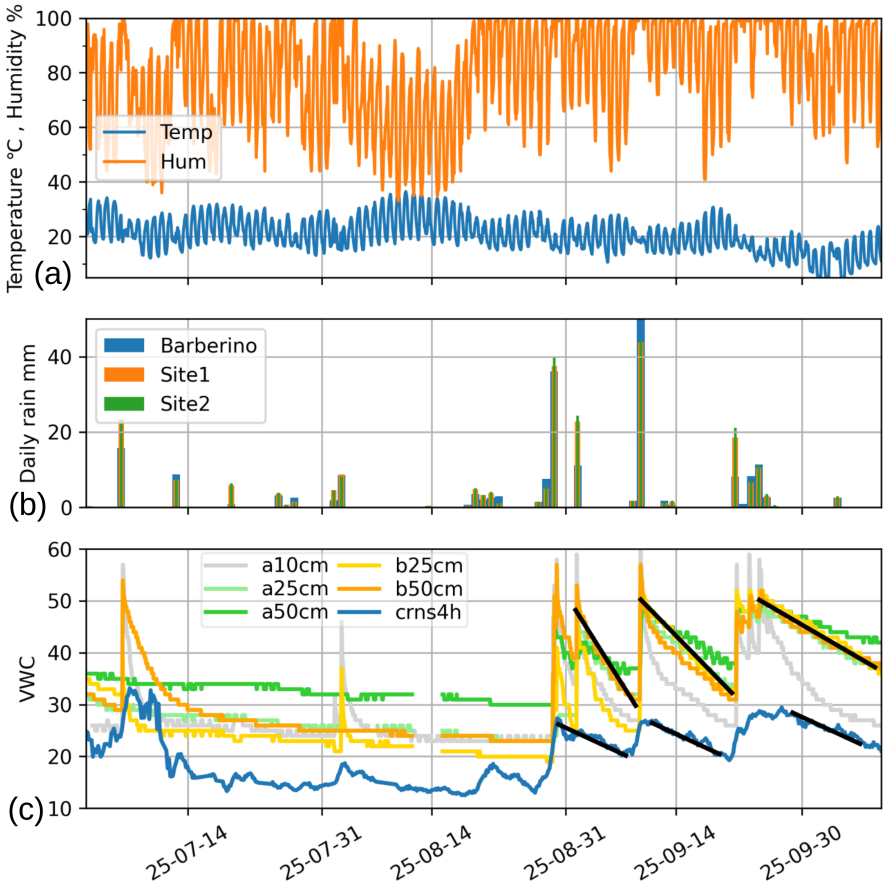


Figure 7: Time series from July to October 2025. The black segments highlight the changing drying rate with decreasing temperature and radiation. The linear segments for the CRNS series appear shifted but not rotated, highlighting how the drying rates (the angles) did not change over the three periods.

https://doi.org/10.5194/egusphere-2026-5633
Preprint. Discussion started: 11 November 2026
© Author(s) 2026. CC BY 4.0 License.

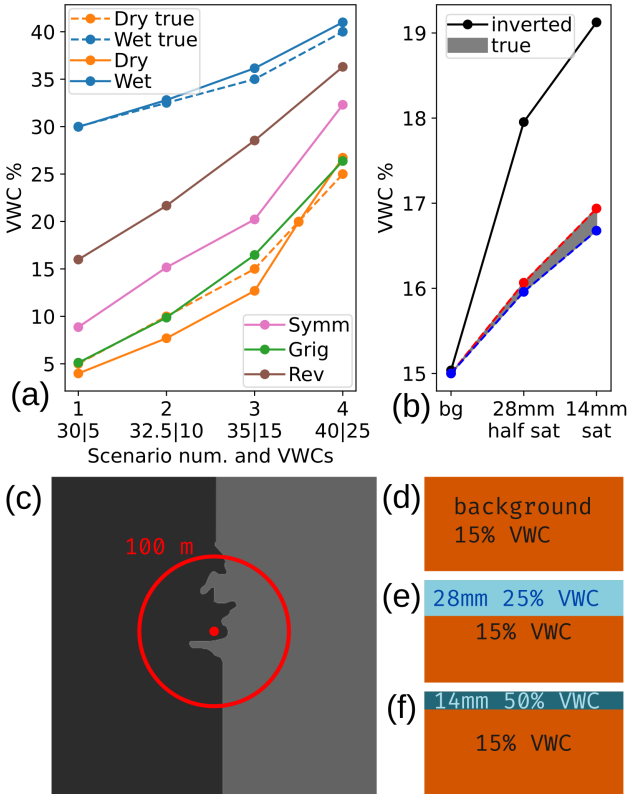


Figure 8: CRNS numerical simulations of different scenarios with lateral (a) and vertical (b) VWC variability (Tab. 1). (a) The Dry and Wet sets represent the initial homogeneous tests. The dashed lines are the true input VWC values (URANOS), and the solid lines show the VWC values resulting from the URANOS-CoRNy simulations. The Grignanello (Gri), Reverse (Rev), and Symmetric (Sym) heterogeneous scenarios (VWC values on x-axis) illustrate the high sensitivity to the dry region, even when the detector is near the boundary (Gri, Sym) or within the wet region (Rev), see text. (b) shows the high sensitivity of the CRNS to increasing VWC at the soil surface (d, e, f). The continuous line shows the VWC values returned by the URANOS-CoRNy simulations. The dashed lines show the VWC calculated by distributing 7 mm of water over the estimated depths of the footprints, considering the background model (blue, 29.1 cm) or scenarios with top water (red, 22.6 and 14.4 cm, respectively). (c) Two-domain model derived from the geophysical results.

https://doi.org/10.5194/egusphere-2026-5633
Preprint. Discussion started: 11 November 2026
© Author(s) 2026. CC BY 4.0 License.

geometrical aspects. Despite the symmetry, the CRNS response remains significantly closer to the curve of the dry region. Together, the scenarios quantify the dominance of the dry region, even when the detector is near the boundary (Gri, Sym) or within the wet region (Rev).

Figure 8b shows the simulation results of the second set, exploring the CRNS sensitivity to increasing VWC at the soil surface. To simulate a light rainfall event, a thin topsoil layer with higher VWC was added at the top of a homogeneous background model with 15 % VWC (Fig. 8d). This top layer contains 7 mm of water distributed over a thickness of 28 mm in Fig. 8e (VWC of 25 %) and 14 mm in Fig. 8f (full saturation, VWC of 50 %). The dashed lines show the VWC calculated by distributing the 7 mm of water over the estimated footprint depths from URANOS, considering the background model (blue, 29.1 cm) or scenarios with top water (red, 22.6 and 14.4 cm, respectively). While the depth-integrated VWC of the three models is similar, the CRNS response is highly sensitive to the near-surface VWC, resulting in amplified differences and overestimated VWC values of 18 % and 19 %. This scenario shows how a light rain may be well captured by the CRNS time series, but has no effect even on relatively shallow soil sensors, particularly under strong ET or with dry and low-permeability soil (Fig. 7).

4 Discussion

The geophysical characterizations of the study site agree on the presence of two domains, with an irregular, fingering transition to a more electrically resistive region to the west. This distinction appears similar in both November and April results, suggesting a relevant contribution from the subsurface properties, beyond the temporary VWC conditions. Based on the electrical resistivities and geological information, the lower resistivities (10 to 15 Ω m) suggest higher clay contents, attributable to the argillite or resulting clayey sediments (Fig. A.1). The higher resistivities suggest a more cemented, rockier substrate with lower clay content. Excluding a dominant sandy component, these values are attributable to the marls and marly limestones, but with significant fracture-karstic porosity, as the resistivity (≈45 Ω m) remains low for a more compact rock (Casado et al., 2015; Mebrahtu et al., 2020). In addition to the resistivity values, their spatial patterns captured by the ERT sections strongly resemble the karstic soil-rock interface imaged by Cheng et al. (2019).

The combination of FDEM and multi-scale ERT offered significant advantages over the individual solutions. The FDEM survey conveniently mapped the entire field using a small and light instrument such as the Mini-Explorer. The multi-scale ERT enabled a robust calibration of the Mini-Explorer maps by covering both the lateral resistivity changes and the high-resolution vertical variability in the topsoil. In turn, the ERT-calibrated FDEM extended the geophysical interpretation to the whole plot (Fig. 2). Together, they captured the lateral variability between the two domains at the tens of meters, and the vertical variability at tens of centimeters, from a more homogenized-worked layer to a deeper layer with stronger resistivity contrasts. While the concept of "field-scale" has been central in environmental geophysics (Binley et al., 2015), the possible need for multiple scales often remains undervalued, for example, preferring a single compromise between ERT lateral coverage and vertical resolution (Romero-Ruiz et al., 2025). Instrument characteristics and methodological habits, often attributable to other geophysical applications, still influence the difficult trade-off between number of methods, surveys, and scales (Vereecken et al., 2006), and thus the targeting of scale-specific questions and subsurface processes (Rentschler et al., 2020; Brogi et al., 2019; Carrera et al., 2024).

https://doi.org/10.5194/egusphere-2026-5633
Preprint. Discussion started: 11 November 2026
© Author(s) 2026. CC BY 4.0 License.

The soil sensors were installed within an intrusion of the clayey domain. This installation reflected an initial assumption of relatively homogeneous conditions, driven by the visual appearance of the topsoil, and convenient access from the south side of the plot. In contrast, the CRNS detector was located in the marly domain, although just about 18 m north of the soil sensors. This different location was chosen by balancing the proximity to the soil sensors and a more central position within the plot, in light of the detector footprint (Brogi et al., 2023; Köhli et al., 2015). While this is a study-specific issue, it highlights how different groups within a multidisciplinary project may prioritize different aspects and locations, unless informed otherwise (Cocozza and Penna, 2022).

The results motivated a deeper discussion of the VWC time series and their differences. In winter, the higher and more stable VWC values from the soil sensors contrast with the lower and more responsive CRNS time series. Because of the low winter ET, the fluctuations of the CRNS are likely dominated by infiltration processes. On the contrary, the high (≈45 %) and stable VWC of the soil sensors suggest lower permeabilities and high water holding capacity, compatible with higher clay contents (Carsel and Parrish, 1988; Wösten et al., 1999). In June, the CRNS series drops earlier and faster, even in the first and cooler week, while the soil sensors decrease later and more slowly, better matching the temperature increase. This difference appears consistent with the winter period, i.e., contrasting ET-driven and infiltration-driven dynamics. In summer and fall, the CRNS series maintains lower VWC values but the soil sensors show stronger dynamics in this period. Because of the high ET, the response of the soil sensors is compatible with an upper and more permeable layer above a low-permeability substrate. Together, the two layers would allow the water to infiltrate to the sensors but then hinder deeper infiltration, resulting in the strong increases of VWC. The drying curves would then be dominated by the ET, as possibly indicated by the diminishing steepness from September onwards. In contrast, the CRNS series is compatible with a more permeable substrate.

The combination of VWC monitoring and geophysical results depicts a conceptual model that distinguishes a homogeneous-worked soil above a more heterogeneous substrate. The shallow layer of about 30 to 50 cm is more homogenized, with permeability typical of a silt loam with low-normal compaction, given by light machinery and natural porosity associated with macro organisms and roots (see also Fig. A.1). In contrast, the deeper substrate distinguishes a karstic-fractured marl and clay domains (i.e., the marly and clayey regions), with the expected strong permeability contrasts. While this study limited its focus to textural differences, several other aspects can lead to spatiotemporal soil variability, for example rocky fragments and substrates (Zhang et al., 2016), plant roots, and morphology (Hubbard et al., 2021). This conceptual model motivated the numerical analyses of the CRNS sensitivity to its relative position within the marly domain, and to light rain and associated water layer on soil or vegetation surface.

The numerical simulations (Tab. 1 and Fig. 8) provided insight into the nonlinearity and nonuniqueness of the CRNS data (Zreda et al., 2012). The simulations exploring the lateral dry-dominance (Set I) support the observed differences between the VWC time series of the soil sensors and CRNS. Such differences characterized the VWC series over the entire year of monitoring, reaching up to 20 % VWC. Furthermore, the above conceptual model, even in its simplicity, suggests that the captured complexity of the VWC dynamics goes beyond the simple dry-dominance and average discrepancy. For example, CRNS and soil sensors responded differently to precipitations, depending on season, soil conditions, and precipitation characteristics (Figs. 5, 6, 7). From a CRNS viewpoint, this reflects the complex interplay of CRNS lateral and vertical sensitivities, and spatiotemporal VWC

https://doi.org/10.5194/egusphere-2026-5633
Preprint. Discussion started: 11 November 2026
© Author(s) 2026. CC BY 4.0 License.

dynamics under variable drainage efficiency (e.g., marly and clayey regions) and ET (i.e., seasonality).

This aspect was already noted by Schrön et al. (2017), who highlighted how inappropriate averaging approaches could hinder CRNS interpretations. The authors focused on surface aspects, such as vegetation and soil ponding, to make the relationship between CRNS and soil moisture dynamics more physically based. Subsequent studies further highlighted the importance of other surface features, including dry roads in agricultural environments (Schrön et al., 2018) and snow-free patches in otherwise snow-covered areas (Schattan et al., 2019). Our study aligns with the above and shows how CRNS may be significantly affected even in the absence of clear surface clues, i.e., with relatively homogeneous soil texture and vegetation types. The results also highlight how different field heterogeneity or installation setups would have equally challenged the VWC monitoring. For example, the reverse scenario (Rev in Fig. 8) suggests that apparent inconsistencies would have been faced even if the CRNS had been positioned together with the soil sensors. In addition, co-positioning and relative soil homogeneity around the installation may undervalue similar concerns and investigations regarding the spatial heterogeneity. These observations motivated the numerical and theoretical generalization of the dry-dominance presented in Section 5.

Recent studies explored more spatially-aware CRNS solutions (Rasche et al., 2021; Köhli, 2026), including roving (Baatz et al., 2017; Schrön et al., 2018; Zhang et al., 2024) and network solutions (Brogi et al., 2026; Heistermann et al., 2023) at the watershed or field scale, and directional shielding (Francke et al., 2022). However, the "field of view of the probe is diluted" by the neutron scattering itself, and common sensor count rates further limit easy spatial resolution gains (Jakobi et al., 2020). Hence, while our study supports similar CRNS-based advances, the integration of field geophysical characterizations remains relevant to inform CRNS models and their interpretations (Brogi et al., 2019). In directional, roving, or network solutions, the model complexity would need to be balanced against CRNS acquisition times, network optimization, and rover logistics (Franz et al., 2015; Jakobi et al., 2020). Data assimilation approaches integrating soil and weather data would likely be advantageous and address spatiotemporal VWC dynamics that would otherwise remain elusive, even with better constrained models (Baatz et al., 2017). For example, the coupling with precipitation and ET data could help interpret the amplified CRNS sensitivity to VWC dynamics in dry regions and light precipitation events (Franz et al., 2012). While the resulting VWC estimates are overestimated (Figs. 7 and 8), they capture surface moisture dynamics that soil sensors typically miss, and thus remain physically meaningful when interpreted within a soil hydrology model. Beyond the focus on footprint heterogeneity, this study shifts the focus toward CRNS nonlinearity and consequent dry-dominance, which remains even when the footprint weighting is accounted for. Dry-dominance is further explored and generalized beyond the study site in the next section.

Regarding the CRNS vertical sensitivity, Scheiffele et al. (2020) proposed a vertical profile correction to rescale the CRNS vertical sensitivity using moisture profiles obtained from nearby soil sensors. Based on their work on four distinct sites and literature review, the authors recommended using one profile location near the CRNS probe (<100 m), while also discussing the possibility of additional point measurements for field sites with pronounced heterogeneity. On the one hand, our study provides new numerical and field-based evidence of the implications of the CRNS sensitivity, supporting the motivation and findings of Scheiffele et al. (2020), even when the significance of the lateral and vertical variability is less apparent. On the other hand, this work highlights

https://doi.org/10.5194/egusphere-2026-5633
Preprint. Discussion started: 11 November 2026
© Author(s) 2026. CC BY 4.0 License.

that improving, comparing, and correcting CRNS and soil sensors must go hand in hand with the understanding of site-specific spatiotemporal hydrological dynamics. This way, soil sensors and CRNS data can effectively complement each other, mitigating the unavoidable effects of natural complexity and the biases introduced when correcting integrated measurements with point measurements. For example, Scheiffele et al. (2020) also reported how their correction was especially relevant for pronounced wetting and drying fronts. While our seasonal results agree on this, they also highlight how the relevance of CRNS corrections is inherently linked to the site complexity, and thus challenges in defining a suitable and representative correction.

In their opinion paper, Nasta et al. (2025) advocated for more in-depth hydrological investigations addressing the complexity of nonlinear processes modulated by scale-dependent feedback and multiscale spatiotemporal variability. This study reinforces the above rationale, even with the relatively small field scale and simple conceptual model. Regarding the economical and organizational aspects considered by Nasta et al. (2025), our results show that geophysical characterizations would valuably contribute to the proposed hydrological observatory at the catchment scale. The geophysical surveys occupied three people for three days, with instrumentation cost ranging between 100 000 and 130 000 euros, to be amortized over more than a decade. Such costs would often be justified given the resource investment for establishing and capitalizing the proposed long-term hydrological observatories (Bogena et al., 2018; Nasta et al., 2025; Köhli, 2026). The recent development of open-source and low-cost ERT instruments will further support the integration of ERT characterizations, but especially monitoring, in hydrological studies and observatories (Blanchy et al., 2024; Watlet et al., 2023; Clement et al., 2020).

5 Numerical and theoretical generalization of dry dominance

By Jensen's inequality, the strictly decreasing and convex shape ($f'(\theta) < 0, f''(\theta) > 0$) of the UTS function implies that averaging in soil-moisture space is not equivalent to averaging in neutron-intensity space. That is, it implies that the resulting CRNS estimate is systematically biased toward drier moisture values. This physical bias is distinct from the geometric bias arising from the CRNS sensor position and footprint sensitivity. While the footprint-geometric bias can be positive, negative, or null, the dry-dominance bias is strictly negative, and vanishes only under homogeneous conditions. Considering the three numerical scenarios (Gri, Rev, Sym), Gri has both biases negative and thus additive, Sym has only the dry-dominance bias, and the geometric bias becomes positive in Rev.

Let w_i be the normalized footprint weight of compartment i, and let $N(\theta_i)$ be the neutron intensity associated with its VWC θ_i (Eq. 1). In the following, N^{-1} denotes the inverse of the UTS function, with the same parametrization. The effective CRNS signal is

$$N_{\text{eff}} = \sum_i w_i N(\theta_i)\,. \tag{2}$$

The corresponding signal contribution of compartment i is

$$c_i = \frac{w_i N(\theta_i)}{\sum_j w_j N(\theta_j)}\,. \tag{3}$$

The distinction between w_i and c_i quantifies the difference between footprint-geometric and dry-dominance biases. The weights w_i describe where the signal originates in the

https://doi.org/10.5194/egusphere-2026-5633
Preprint. Discussion started: 11 November 2026
© Author(s) 2026. CC BY 4.0 License.

geometric footprint space. The contributions c_i describe how strongly each compartment contributes to the detected neutron intensity after the nonlinear neutron-moisture transfer function $N(\theta)$ has acted. Consequently, a dry compartment has $c_i > w_i$.

The CRNS-derived effective soil moisture θ_{eff} is obtained by applying the inverse of the UTS function N^{-1} to the effective CRNS signal N_{eff}

$$\theta_{\text{eff}} = N^{-1}(N_{\text{eff}})\,. \tag{4}$$

If the moisture-neutron transfer function were linear, θ_{eff} would be equal to the footprint-weighted mean of the soil moisture,

$$\theta_{\text{fpw}} = \sum_i w_i \theta_i\,. \tag{5}$$

Because $N(\theta)$ is not linear but convex

$$\theta_{\text{eff}} < \theta_{\text{fpw}} \tag{6}$$

in heterogeneous conditions.

The dry-dominance bias is therefore defined as

$$B_{\text{dry}} = \theta_{\text{eff}} - \theta_{\text{fpw}}\,, \tag{7}$$

and persists even after the geometric footprint weighting has been accounted for.

Based on the three scenarios (Gri, Rev, Sym) and increasing VWC contrasts between the two domains, Fig. 9 shows the differences between the geometric mean VWC θ_{geo}, the footprint-weighted VWC θ_{fpw}, and the CRNS-inverted θ_{eff}. The footprint radii were estimated from the homogeneous URANOS simulations by fitting the R_{86} radius (the 86th percentile of the signal distribution) at the simulated VWC values. The footprint weights as a function of the radial distance r were then calculated with $W(r, h, \theta) \approx e^{-2r/R_{86}(h,\theta)}$ (Köhli, 2026). The figure shows how the bias between θ_{eff} and the unweighted geometric mean increases superlinearly with increasing moisture contrasts and decreasing moisture baseline (global moisture arithmetic mean). The θ_{eff} bias (colored lines) is negative and reaches values of about −8 % VWC for a moisture contrast of 25 % and a moisture baseline of 15 % (i.e., domains with 2.5 and 27.5 % VWC). Extending the moisture contrasts to 30 and 35 %, beyond the hydrology-based URANOS simulations (Tab. 1), yields θ_{eff} biases larger than 10 %. In contrast, θ_{fpw} (gray lines) shows a linear behavior dominated by the increasing moisture contrasts. As expected, its bias values are negative, positive, and null for Gri, Rev, Sym, respectively, and remain lower than 1 % VWC. Because the θ_{eff} bias combines both the geometric and dry-dominance biases, it can become positive when the geometric bias is positive and sufficiently large, i.e., when the dry regions do not have enough footprint weight or are not sufficiently dry for the nonlinearity effects to dominate. This was confirmed by moving the sensor location 25 meters into the wet region in the symmetric scenario (Fig. 9d).

The third-order Taylor expansion of the UTS function allows generalizing the dry-dominance DD to statistical distributions of soil moisture, expressed in terms of variance and skewness.

https://doi.org/10.5194/egusphere-2026-5633
Preprint. Discussion started: 11 November 2026
© Author(s) 2026. CC BY 4.0 License.

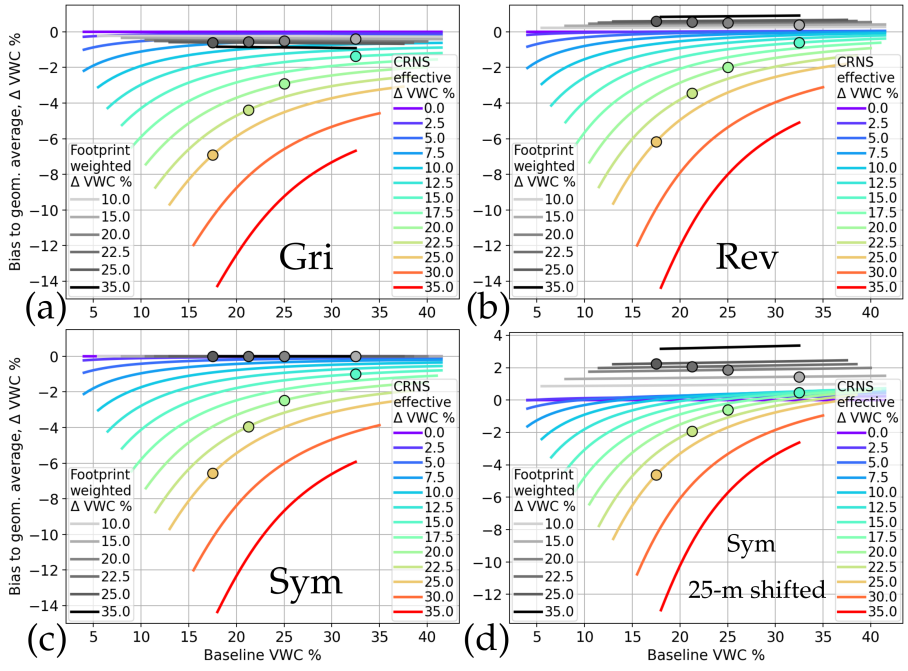


Figure 9: CRNS effective bias (colored lines) and its footprint-geometric (gray colorscale) component for moisture contrasts ranging from 0.1 to 35 % over the possible range of moisture baseline. The percentage bias is calculated relative to the unweighted arithmetic mean of the moisture over the entire model. The geometry of the models (Gri, Rev, Sym) corresponds to the URANOS simulations (Fig. 8 and Tab. 1). (d) shows an additional symmetric scenario with the sensor moved into the wet region, at 25 m from the interface with the dry domain. This scenario shows large positive footprint biases that exceed the nonlinearity dry-dominance effect for relatively wet moisture baselines.

https://doi.org/10.5194/egusphere-2026-5633
Preprint. Discussion started: 11 November 2026
© Author(s) 2026. CC BY 4.0 License.

$$\mathrm{DD} \approx \mathrm{DD2} \quad \mathrm{DD3} \tag{8}$$

$$\approx \frac{1}{2}\frac{N''}{N'}\sum_i w_i(\theta_i - \mu_w)^2 \quad \frac{1}{6}\frac{N'''}{N'}\sum_i w_i(\theta_i - \mu_w)^3 \tag{9}$$

$$\approx \frac{1}{2}K_2\sigma_w^2 \quad \frac{1}{6}K_3\gamma_w\sigma_w^3 \tag{10}$$

where DD2 and DD3 are the second- and third-order bias terms, μ_w the footprint-weighted mean moisture, σ_w^2 is the weighted variance, and γ_w the weighted skewness. K_2 and K_3 quantify the nonlinearity effect through the second and third derivatives (N'' and N'''), and thus the dependence on the moisture baseline. $(\theta_i - \mu_w)^2$ and $(\theta_i - \mu_w)^3$ generalize and parameterize the moisture distribution through its second and third moments. The second-order term directly expresses Jensen's inequality and is central to the generalization of the dry-dominance. Nonetheless, the third-order term and its skewness dependence is included here because it physically captures the effect of relatively very dry (e.g., roads) and very wet (ponding, snow) on the moisture distribution.

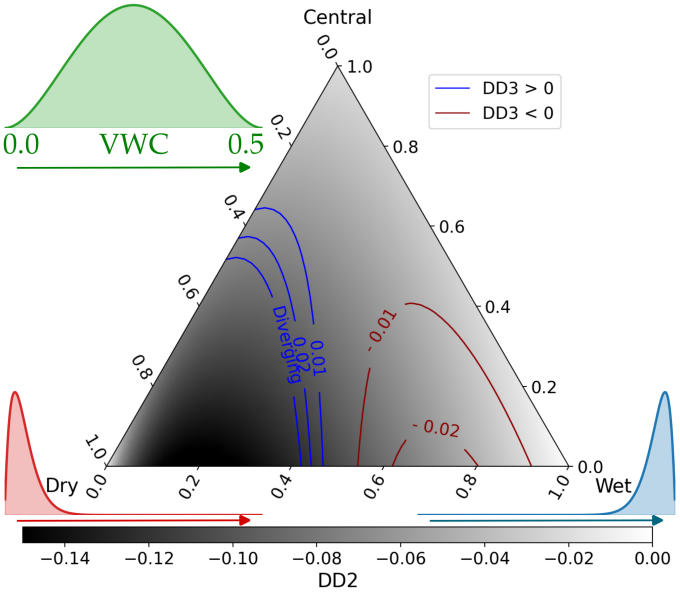


Figure 10: Statistical generalization of the dry-dominance combining three beta distributions (dry, central, wet) of soil moisture. The resulting combination spans a wide range of moisture distributions, in terms of mean moisture, variance, and skewness. The second-order bias term (DD2) is negative and its magnitude increases toward the bottom-left corner, i.e., with increasing variance (moisture variability) and slope of the UTS function. The contour lines show how the third-order term varies with the skewness and thus has negative values on the right and positive on the left (see text).

Figure 10 visualizes the analytical generalization using three beta distributions, representing a central soil moisture distribution (central, $\alpha = \beta = 3$), a dry region ($\alpha = 2, \beta = 25$),

https://doi.org/10.5194/egusphere-2026-5633
Preprint. Discussion started: 11 November 2026
© Author(s) 2026. CC BY 4.0 License.

and a wet region ($\alpha = 25, \beta = 2$). The beta distribution was chosen because it is intrinsically bounded and its statistical moments can be calculated analytically. Rescaling between 0 and 0.5 yielded $\mu = 0.250$ for the central distribution, $\mu = 0.037$ for the dry, and $\mu = 0.463$ for the wet, as shown in the figure. The ternary weights vary over the plot to encompass a wide spectrum of field conditions, including unimodal, symmetric, skewed, and strongly bimodal moisture distributions. For example, the mean moisture increases left to right, while the variance increases downward as the dry and wet distributions get more weight. Along the central bisector, a relatively even distribution of the moisture is obtained when the central distribution has a weight of 0.7. In contrast, the bottom edge reproduces bimodal dry-wet distributions and thus the maximum values of variances and DD2. While the variance is maximum at the center of the bottom edge, the DD2 bias further increases to the left because of its K_2 dependence. The dry-dominance estimates observed for bimodal distributions are comparable and consistent with the numerical results for the Sym scenario in Fig. 9, both reaching values larger than 10 %. On the right side, the negative skewness of the distribution results in a negative DD3 which marginally adds to the total DD. The opposite DD3 effect is observed on the left side, where DD3 subtracts from DD2. The DD3 range was limited and its values are not shown at low VWC because the UTS model has a mathematical pole close to zero, causing the third- and higher-order derivatives to grow superlinearly as the moisture approaches zero.

The numerical and analytical generalizations demonstrate that the CRNS count rate is not a footprint-weighted average in soil-moisture space, but a footprint-weighted mixture in neutron-intensity space followed by nonlinear inversion. While the URANOS-CoRNy simulations are numerically more rigorous (e.g., irregular footprint shapes), this section provides a conceptually streamlined and general framework to couple spatial information and CRNS, with potential for guiding future correction and inversion approaches.

6 Conclusions

This field study combined VWC monitoring with soil sensors and CRNS, geophysical characterizations, and CRNS numerical simulations, to compare and understand soil moisture dynamics in a Mediterranean vineyard. The multi-scale ERT and FDEM mapping highlighted a fingering transition from a clayey substrate to a fractured-karstic marl, both overlain by a more worked, homogeneous soil. Together with ancillary weather data, this spatial information and associated infiltration dynamics explained how CRNS and nearby soil sensors responded differently to precipitation, depending on season, soil conditions, and rainfall characteristics. This highlighted the critical interplay between spatiotemporal soil VWC dynamics and CRNS signal nonlinearity and nonuniqueness. CRNS numerical modelling further investigated such interplay, specifically in terms of lateral dry-dominance and amplified sensitivity to light rainfall events. The dry-dominance bias was further generalized numerically and theoretically, showing that the CRNS count rate is not a footprint-weighted average in soil-moisture space, but a footprint-weighted mixture in neutron-intensity space followed by nonlinear inversion. This bias is strictly negative and scales with the variance and skewness of the soil moisture distribution. Together, field observations and numerical modelling informed a conceptual soil hydrology model describing the observed VWC spatiotemporal dynamics. The results reinforce the value of more spatially informed, hydrology-based CRNS applications, a key step toward capitalizing on recent CRNS methodological advances and achieving a better integration with soil moisture networks and multi-methodological hydrological observatories.

https://doi.org/10.5194/egusphere-2026-5633
Preprint. Discussion started: 11 November 2026
© Author(s) 2026. CC BY 4.0 License.

Appendix



Figure A.1: Trench in the clayey domain. The picture shows a thick and fine-textured substrate and a possibly less compacted soil. This supports the geophysical interpretation of the low electrical resistivities (15 Ω m).

Acknowledgements

The authors gratefully acknowledge the hospitality, availability, and support provided by owners and staff of Borgo Grignanello, especially Charlie. The authors thank Alberto Carrera, Jacopo Boaga, Lorenzo Brilli, and Christian Massari for the positive and fruitful discussions. The authors thank Silvia Cattò for helping with the laboratory analysis of soil samples.

Financial support

The authors acknowledge The Geosciences for Sustainable Development project, Budget Ministero dell'Università e della Ricerca Dipartimenti di Eccellenza 2023 – 2027

https://doi.org/10.5194/egusphere-2026-5633
Preprint. Discussion started: 11 November 2026
© Author(s) 2026. CC BY 4.0 License.

C93C23002690001. Additional support came from the RETURN Extended Partnership and received funding from the European Union Next-GenerationEU (National Recovery and Resilience Plan – NRRP, Mission 4, Component 2, Investment 1.3 – grant no. D.D. 1243 2/8/2022, PE0000005). PB acknowledges support from the SNSF Grant number IZCOZ0_205439/1 for the instrumentation of the experimental vineyard.

Author contribution

Conceptualization: LP, GC, VC, JW, MK. Data Curation: LP, VC, JW, PB, MP, FM. Investigation: LP, VC, MP, MC, JW, MK, GC, FM, DP. Methodology: LP, VC, JW, MC. Writing (original draft preparation): LP. Writing (review and editing): LP, VC, GC, MK, JW, MP, MC, PB, DP. Funding acquisition: GC, PB.

Code and data availability

Data used to obtain the results presented in this work can be accessed on the Zenodo open-source repository `https://doi.org/10.5281/zenodo.21003854`, Peruzzo, 2026.

Competing interests

MK and JW hold CEO positions at StyX Neutronica Gmbh, Germany.

References

Ahrens, J., Geveci, B., and Law, C.: ParaView: An End-User Tool for Large-Data Visualization, in: Visualization Handbook, pp. 717–731, Elsevier, ISBN 978-0-12-387582-2, https://doi.org/10.1016/B978-012387582-2/50038-1, 2005.

Atekwana, E. A. and Slater, L. D.: Biogeophysics: A New Frontier in Earth Science Research, Reviews of Geophysics, 47, RG4004, https://doi.org/10.1029/2009RG000285, 2009.

Baatz, R., Hendricks Franssen, H.-J., Han, X., Hoar, T., Bogena, H. R., and Vereecken, H.: Evaluation of a Cosmic-Ray Neutron Sensor Network for Improved Land Surface Model Prediction, Hydrology and Earth System Sciences, 21, 2509–2530, https://doi.org/10.5194/hess-21-2509-2017, 2017.

Babaeian, E., Sadeghi, M., Jones, S. B., Montzka, C., Vereecken, H., and Tuller, M.: Ground, Proximal, and Satellite Remote Sensing of Soil Moisture, Reviews of Geophysics, 57, 530–616, https://doi.org/10.1029/2018RG000618, 2019.

Beven, K.: Environmental Modelling: An Uncertain Future?, Taylor and Francis, London, ISBN 978-0-415-45759-0, https://doi.org/10.1201/9781482288575, 2008.

Binley, A. and Daily, W.: Regularised Image Reconstruction of Noisy Electrical Resistance Tomography Data, in: Process Tomography, 4th Workshop of the European Concerted Action on Process Tomography, pp. 401–410, Bergen, 1995.

Binley, A., Hubbard, S. S., Huisman, J. A., Revil, A., Robinson, D. A., Singha, K., and Slater, L. D.: The Emergence of Hydrogeophysics for Improved Understanding of Subsurface Processes over Multiple Scales: The Emergence of Hydrogeophysics, Water Resources Research, 51, 3837–3866, https://doi.org/10.1002/2015WR017016, 2015.

https://doi.org/10.5194/egusphere-2026-5633
Preprint. Discussion started: 11 November 2026
© Author(s) 2026. CC BY 4.0 License.



Blanchy, G., Saneiyan, S., Boyd, J., McLachlan, P., and Binley, A.: ResIPy, an Intuitive Open Source Software for Complex Geoelectrical Inversion/Modeling, Computers & Geosciences, 137, 104 423, https://doi.org/10.1016/j.cageo.2020.104423, 2020.

Blanchy, G., Watlet, A., Clément, R., Kaufmann, O., Forquet, N., and Guyard, H.: OhmPi: Learn How to Build an Open-Source Resistivity Meter, in: Agriculture and Geophysics: Illuminating the Subsurface, p. 33, Agrogeophysics, https://doi.org/10.62329/MCKV3023, 2024.

Boaga, J.: The Use of FDEM in Hydrogeophysics: A Review, Journal of Applied Geophysics, 139, 36–46, https://doi.org/10.1016/j.jappgeo.2017.02.011, 2017.

Bogena, H., White, T., Bour, O., Li, X., and Jensen, K.: Toward Better Understanding of Terrestrial Processes through Long-Term Hydrological Observatories, Vadose Zone Journal, 17, 1–10, https://doi.org/10.2136/vzj2018.10.0194, 2018.

Bonsall, J., Fry, R., Gaffney, C., Armit, I., Beck, A., and Gaffney, V.: Assessment of the CMD Mini-Explorer, a New Low-Frequency Multi-Coil Electromagnetic Device, for Archaeological Investigations: Assessment of the CMD Mini-Explorer Low-Frequency Electromagnetic Device, Archaeological Prospection, 20, 219–231, https://doi.org/10.1002/arp.1458, 2013.

Boyd, J. P., Chambers, J. E., Wilkinson, P. B., Meldrum, P. I., Bruce, E., and Binley, A.: Coupled Hydrogeophysical Modeling to Constrain Unsaturated Soil Parameters for a Slow-Moving Landslide, Water Resources Research, 60, e2023WR036 319, https://doi.org/10.1029/2023WR036319, 2024.

Brogi, C., Huisman, J., Pätzold, S., Von Hebel, C., Weihermüller, L., Kaufmann, M., Van Der Kruk, J., and Vereecken, H.: Large-Scale Soil Mapping Using Multi-Configuration EMI and Supervised Image Classification, Geoderma, 335, 133–148, https://doi.org/10.1016/j.geoderma.2018.08.001, 2019.

Brogi, C., Pisinaras, V., Köhli, M., Dombrowski, O., Hendricks Franssen, H.-J., Babakos, K., Chatzi, A., Panagopoulos, A., and Bogena, H. R.: Monitoring Irrigation in Small Orchards with Cosmic-Ray Neutron Sensors, Sensors, 23, 2378, https://doi.org/10.3390/s23052378, 2023.

Brogi, C., Nieberding, F., Scheiffele, L., Daccache, A., Schrön, M., and Bogena, H. R.: Irrigation Monitoring With Cosmic-Ray Neutron Sensors: Unraveling Field Experiments With Neutron Transport Simulations, Water Resources Research, 62, e2025WR043 105, https://doi.org/10.1029/2025WR043105, 2026.

Brunet, P., Clément, R., and Bouvier, C.: Monitoring Soil Water Content and Deficit Using Electrical Resistivity Tomography (ERT) – A Case Study in the Cevennes Area, France, Journal of Hydrology, 380, 146–153, https://doi.org/10.1016/j.jhydrol.2009.10.032, 2010.

Byrd, R. H., Lu, P., Nocedal, J., and Zhu, C.: A Limited Memory Algorithm for Bound Constrained Optimization, SIAM Journal on Scientific Computing, 16, 1190–1208, https://doi.org/10.1137/0916069, 1995.

Callesen, I., Keck, H., and Andersen, T. J.: Particle Size Distribution in Soils and Marine Sediments by Laser Diffraction Using Malvern Mastersizer 2000—Method Uncertainty Including the Effect of Hydrogen Peroxide Pretreatment, Journal of Soils and Sediments, 18, 2500–2510, https://doi.org/10.1007/s11368-018-1965-8, 2018.

Carmignani, L., Conti, P., Cornamusini, G., and Pirro, A.: Geological Map of Tuscany (Italy), Journal of Maps, 9, 487–497, https://doi.org/10.1080/17445647.2013.820154, 2013.

Carrera, A., Peruzzo, L., Longo, M., Cassiani, G., and Morari, F.: Uncovering Soil Compaction: Performance of Electrical and Electromagnetic Geophysical Methods, SOIL, 10, 843–857, https://doi.org/10.5194/soil-10-843-2024, 2024.

Carsel, R. F. and Parrish, R. S.: Developing Joint Probability Distributions of Soil Water Retention Characteristics, Water Resources Research, 24, 755–769, https://doi.org/10.1029/WR024i005p00755, 1988.

https://doi.org/10.5194/egusphere-2026-5633
Preprint. Discussion started: 11 November 2026
© Author(s) 2026. CC BY 4.0 License.



Casado, I., Mahjoub, H., Lovera, R., Fernández, J., and Casas, A.: Use of Electrical Tomography Methods to Determinate the Extension and Main Migration Routes of Uncontrolled Landfill Leachates in Fractured Areas, Science of The Total Environment, 506–507, 546–553, https://doi.org/10.1016/j.scitotenv.2014.11.068, 2015.

Cheng, Q., Tao, M., Chen, X., and Binley, A.: Evaluation of Electrical Resistivity Tomography (ERT) for Mapping the Soil–Rock Interface in Karstic Environments, Environmental Earth Sciences, 78, 439, https://doi.org/10.1007/s12665-019-8440-8, 2019.

Clement, R., Fargier, Y., Dubois, V., Gance, J., Gros, E., and Forquet, N.: OhmPi: An Open Source Data Logger for Dedicated Applications of Electrical Resistivity Imaging at the Small and Laboratory Scale, HardwareX, 8, e00 122, https://doi.org/10.1016/j.ohx.2020.e00122, 2020.

Cocozza, C. and Penna, D.: Towards a More Active Dialogue between Hydrologists and Ecophysiologists for Interdisciplinary Studies in Forest Ecosystems, Science of The Total Environment, 807, 150 877, https://doi.org/10.1016/j.scitotenv.2021.150877, 2022.

Dawson, N., Fischer, J., Kuhn, M., Pasotti, A., Rouzaud, D., mhugent, Bruy, A., Sutton, T., Dobias, M., Pellerin, M., Rouault, E., Olaya, V., Blottiere, P., Macho, W., Cabieces, J., Blazek, R., Bartoletti, L., Sherman, G., Harrissou Sant-anna, Woodrow, N., signedav, Natsis, S., rldhont, Felder, J., Shaffer, L., Belgacem, N., Santilli, S., Larosa, S., Mani, S., and Jurgiel, B.: Qgis/QGIS: 4.2.2, Zenodo, https://doi.org/10.5281/ZENODO.22144220, 2026.

Desilets, D., Zreda, M., and Ferré, T. P. A.: Nature's Neutron Probe: Land Surface Hydrology at an Elusive Scale with Cosmic Rays, Water Resources Research, 46, 2009WR008 726, https://doi.org/10.1029/2009WR008726, 2010.

Evett, S. R., Heng, L. K., Moutonnet, P., and Nguyen, M. L.: Field Estimation of Soil Water Content: A Practical Guide to Methods, Instrumentation, and Sensor Technology, in: Soil and Water Management & Crop Nutrition Section, vol. IAEA-TCS-30 of *30*, p. 131, International Atomic Energy Agency, Vienna, ISSN 1018-5518, 2008.

Francke, T., Heistermann, M., Köhli, M., Budach, C., Schrön, M., and Oswald, S. E.: Assessing the Feasibility of a Directional Cosmic-Ray Neutron Sensing Sensor for Estimating Soil Moisture, Geoscientific Instrumentation, Methods and Data Systems, 11, 75–92, https://doi.org/10.5194/gi-11-75-2022, 2022.

Franz, T. E., Zreda, M., Rosolem, R., and Ferre, T.: Field Validation of a Cosmic-Ray Neutron Sensor Using a Distributed Sensor Network, Vadose Zone Journal, 11, https://doi.org/10.2136/vzj2012.0046, 2012.

Franz, T. E., Wang, T., Avery, W., Finkenbiner, C., and Brocca, L.: Combined Analysis of Soil Moisture Measurements from Roving and Fixed Cosmic Ray Neutron Probes for Multiscale Real-time Monitoring, Geophysical Research Letters, 42, 3389–3396, https://doi.org/10.1002/2015GL063963, 2015.

Garré, S., Hyndman, D., Mary, B., and Werban, U.: Geophysics Conquering New Territories: The Rise of "Agrogeophysics", Vadose Zone Journal, 20, e20 115, https://doi.org/10.1002/vzj2.20115, 2021.

Glover, P. W. J.: A New Theoretical Interpretation of Archie's Saturation Exponent, Solid Earth, 8, 805–816, https://doi.org/10.5194/se-8-805-2017, 2017.

Greacen, E. L., ed.: Soil Water Assessment by the Neutron Method, CSIRO Australia, Melbourne, ISBN 978-0-643-00414-6, 1981.

Guillaume, T., Bragazza, L., Levasseur, C., Libohova, Z., and Sinaj, S.: Long-Term Soil Organic Carbon Dynamics in Temperate Cropland-Grassland Systems, Agriculture, Ecosystems & Environment, 305, 107 184, https://doi.org/10.1016/j.agee.2020.107184, 2021.

https://doi.org/10.5194/egusphere-2026-5633
Preprint. Discussion started: 11 November 2026
© Author(s) 2026. CC BY 4.0 License.



Guillemoteau, J. and Tronicke, J.: Non-Standard Electromagnetic Induction Sensor Configurations: Evaluating Sensitivities and Applicability, Journal of Applied Geophysics, 118, 15–23, https://doi.org/10.1016/j.jappgeo.2015.04.008, 2015.

Heidbüchel, I., Güntner, A., and Blume, T.: Use of Cosmic-Ray Neutron Sensors for Soil Moisture Monitoring in Forests, Hydrology and Earth System Sciences, 20, 1269–1288, https://doi.org/10.5194/hess-20-1269-2016, 2016.

Heiri, O., Lotter, A. F., and Lemcke, G.: Loss on Ignition as a Method for Estimating Organic and Carbonate Content in Sediments: Reproducibility and Comparability of Results, Journal of Paleolimnology, 25, 101–110, https://doi.org/10.1023/A:1008119611481, 2001.

Heistermann, M., Francke, T., Scheiffele, L., Dimitrova Petrova, K., Budach, C., Schrön, M., Trost, B., Rasche, D., Güntner, A., Döpper, V., Förster, M., Köhli, M., Angermann, L., Antonoglou, N., Zude-Sasse, M., and Oswald, S. E.: Three Years of Soil Moisture Observations by a Dense Cosmic-Ray Neutron Sensing Cluster at an Agricultural Research Site in North-East Germany, Earth System Science Data, 15, 3243–3262, https://doi.org/10.5194/essd-15-3243-2023, 2023.

Hoogsteen, M. J. J., Lantinga, E. A., Bakker, E. J., Groot, J. C. J., and Tittonell, P. A.: Estimating Soil Organic Carbon through Loss on Ignition: Effects of Ignition Conditions and Structural Water Loss, European Journal of Soil Science, 66, 320–328, https://doi.org/10.1111/ejss.12224, 2015.

Howard, P. J. A. and Howard, D. M.: Use of Organic Carbon and Loss-on-Ignition to Estimate Soil Organic Matter in Different Soil Types and Horizons, Biology and Fertility of Soils, 9, 306–310, https://doi.org/10.1007/BF00634106, 1990.

Hubbard, S. S., Williams, K. H., Agarwal, D., Banfield, J., Beller, H., Bouskill, N., Brodie, E., Carroll, R., Dafflon, B., Dwivedi, D., Falco, N., Faybishenko, B., Maxwell, R., Nico, P., Steefel, C., Steltzer, H., Tokunaga, T., Tran, P. A., Wainwright, H., and Varadharajan, C.: The East River, Colorado, Watershed: A Mountainous Community Testbed for Improving Predictive Understanding of Multiscale Hydrological–Biogeochemical Dynamics, Vadose Zone Journal, 17, 1–25, https://doi.org/10.2136/vzj2018.03.0061, 2018.

Hubbard, S. S., Schmutz, M., Balde, A., Falco, N., Peruzzo, L., Dafflon, B., Léger, E., and Wu, Y.: Estimation of Soil Classes and Their Relationship to Grapevine Vigor in a Bordeaux Vineyard: Advancing the Practical Joint Use of Electromagnetic Induction (EMI) and NDVI Datasets for Precision Viticulture, Precision Agriculture, https://doi.org/10.1007/s11119-021-09788-w, 2021.

Jakobi, J., Huisman, J. A., Schrön, M., Fiedler, J., Brogi, C., Vereecken, H., and Bogena, H. R.: Error Estimation for Soil Moisture Measurements With Cosmic Ray Neutron Sensing and Implications for Rover Surveys, Frontiers in Water, 2, 10, https://doi.org/10.3389/frwa.2020.00010, 2020.

Köhli, M.: Soil Moisture Measurements by Cosmic-Ray Neutron Sensing: A Critical Review, Geoderma, 465, 117 626, https://doi.org/10.1016/j.geoderma.2025.117626, 2026.

Köhli, M. and Weimar, J.: Beyond Helium-3: Instruments for Cosmic-Ray Neutron Sensing Based on Boron-10 Neutron Detectors, Instruments, 10, 31, https://doi.org/10.3390/instruments10020031, 2026.

Köhli, M., Schrön, M., Zreda, M., Schmidt, U., Dietrich, P., and Zacharias, S.: Footprint Characteristics Revised for Field-scale Soil Moisture Monitoring with Cosmic-ray Neutrons, Water Resources Research, 51, 5772–5790, https://doi.org/10.1002/2015WR017169, 2015.

Köhli, M., Schrön, M., and Schmidt, U.: Response Functions for Detectors in Cosmic Ray Neutron Sensing, Nuclear Instruments and Methods in Physics Research Section A: Accelerators, Spectrometers, Detectors and Associated Equipment, 902, 184–189, https://doi.org/10.1016/j.nima.2018.06.052, 2018.

Köhli, M., Weimar, J., Schrön, M., Baatz, R., and Schmidt, U.: Soil Moisture and Air Humidity Dependence of the Above-Ground Cosmic-Ray Neutron Intensity, Frontiers in Water, 2, 544 847, https://doi.org/10.3389/frwa.2020.544847, 2021.

https://doi.org/10.5194/egusphere-2026-5633
Preprint. Discussion started: 11 November 2026
© Author(s) 2026. CC BY 4.0 License.



Köhli, M., Schrön, M., Zacharias, S., and Schmidt, U.: URANOS v1.0 – the Ultra Rapid Adaptable Neutron-Only Simulation for Environmental Research, Geoscientific Model Development, 16, 449–477, https://doi.org/10.5194/gmd-16-449-2023, 2023.

Li, X.-G., Lv, Y., Ma, B.-G., Wang, W.-Q., and Jian, S.-W.: Decomposition Kinetic Characteristics of Calcium Carbonate Containing Organic Acids by TGA, Arabian Journal of Chemistry, 10, S2534–S2538, https://doi.org/10.1016/j.arabjc.2013.09.026, 2017.

Loveland, P.: Is There a Critical Level of Organic Matter in the Agricultural Soils of Temperate Regions: A Review, Soil and Tillage Research, 70, 1–18, https://doi.org/10.1016/S0167-1987(02)00139-3, 2003.

Lugato, E., Lavallee, J. M., Haddix, M. L., Panagos, P., and Cotrufo, M. F.: Different Climate Sensitivity of Particulate and Mineral-Associated Soil Organic Matter, Nature Geoscience, 14, 295–300, https://doi.org/10.1038/s41561-021-00744-x, 2021.

Mary, B., Peruzzo, L., Boaga, J., Schmutz, M., Wu, Y., Hubbard, S. S., and Cassiani, G.: Small-Scale Characterization of Vine Plant Root Water Uptake via 3-D Electrical Resistivity Tomography and Mise-à-La-Masse Method, Hydrology and Earth System Sciences, 22, 5427–5444, https://doi.org/10.5194/hess-22-5427-2018, 2018.

Masnaghetti, A.: Chianti Classico - Additional Geographic Units, Tech. rep., ENOGEA, Monza, Italy, https://www.enogea.it, 2022.

McLachlan, P., Blanchy, G., and Binley, A.: EMagPy: Open-Source Standalone Software for Processing, Forward Modeling and Inversion of Electromagnetic Induction Data, Computers & Geosciences, 146, 104 561, https://doi.org/10.1016/j.cageo.2020.104561, 2021.

McNeill, J. D.: Electromagnetic Terrain Conductivity Measurement at Low Induction Numbers, Geonics Limited, Technical Note 6, 13, 1980.

Mebrahtu, G., Abay, A., Hailu, G., and Hagos, M.: Electrical Resistivity Imaging and Engineering Geological Investigation of Gereb Segen Dam, Northern Ethiopia, Bulletin of Engineering Geology and the Environment, 79, 83–95, https://doi.org/10.1007/s10064-019-01577-0, 2020.

Nasta, P., Blöschl, G., Bogena, H. R., Zacharias, S., Baatz, R., De Lannoy, G., Jensen, K. H., Manfreda, S., Pfister, L., Tarquis, A. M., Van Meerveld, I., Voltz, M., Zeng, Y., Kustas, W., Li, X., Vereecken, H., and Romano, N.: HESS Opinions: Towards a Common Vision for the Future of Hydrological Observatories, Hydrology and Earth System Sciences, 29, 465–483, https://doi.org/10.5194/hess-29-465-2025, 2025.

Nelson, D. and Sommers, L.: Total Carbon, Organic Carbon, and Organic Matter, in: Agronomy Monographs, edited by Page, A., vol. 9, pp. 539–579, Wiley, 1 edn., ISBN 978-0-89118-072-2 978-0-89118-977-0, https://doi.org/10.2134/agronmonogr9.2.2ed.c29, 1982.

Ney, P., Kohli, M., Bogena, H., and Goergen, K.: CRNS-Based Monitoring Technologies for a Weather and Climate-Resilient Agriculture: Realization by the ADAPTER Project, in: 2021 IEEE International Workshop on Metrology for Agriculture and Forestry (MetroAgriFor), pp. 203–208, IEEE, Trento-Bolzano, Italy, ISBN 978-1-6654-0533-1, https://doi.org/10.1109/MetroAgriFor52389.2021.9628766, 2021.

O'Kelly, B. C.: Method to Compare Water Content Values Determined on the Basis of Different Oven-Drying Temperatures, Géotechnique, 55, 329–332, https://doi.org/10.1680/geot.2005.55.4.329, 2005.

O'Leary, D., Brogi, C., Brown, C., Tuohy, P., and Daly, E.: Linking Electromagnetic Induction Data to Soil Properties at Field Scale Aided by Neural Network Clustering, Frontiers in Soil Science, 4, 1346 028, https://doi.org/10.3389/fsoil.2024.1346028, 2024.

Panagos, P., De Rosa, D., Liakos, L., Labouyrie, M., Borrelli, P., and Ballabio, C.: Soil Bulk Density Assessment in Europe, Agriculture, Ecosystems & Environment, 364, 108 907, https://doi.org/10.1016/j.agee.2024.108907, 2024.

https://doi.org/10.5194/egusphere-2026-5633
Preprint. Discussion started: 11 November 2026
© Author(s) 2026. CC BY 4.0 License.

Peruzzo, L., Chou, C., Hubbard, S., Brodie, E., Uhlemann, S., Dafflon, B., Wielandt, S., Mary, B., Cassiani, G., Morales, A., and Wu, Y.: Outdoor Mesoscale Fabricated Ecosystems: Rationale, Design, and Application to Evapotranspiration, Science of The Total Environment, 957, 177 565, https://doi.org/10.1016/j.scitotenv.2024.177565, 2024.

Peruzzo, L., Werban, U., Pohle, M., Pavoni, M., Mary, B., Cassiani, G., Consoli, S., and Vanella, D.: High-Resolution Frequency-Domain Electromagnetic Mapping for the Hydrological Modeling of an Orange Orchard, SOIL, 11, 811–831, https://doi.org/10.5194/soil-11-811-2025, 2025.

Pini, S., Cassiani, G., Peruzzo, L., Piemontese, L., Dani, A., Giambastiani, Y., and Preti, F.: Sediment Water Storage Investigation of Check Dams Using Electrical Resistivity Tomography, Journal of Hydrology, 665, 134 647, https://doi.org/10.1016/j.jhydrol.2025.134647, 2026.

Raper, R.: Agricultural Traffic Impacts on Soil, Journal of Terramechanics, 42, 259–280, https://doi.org/10.1016/j.jterra.2004.10.010, 2005.

Rasche, D., Köhli, M., Schrön, M., Blume, T., and Güntner, A.: Towards Disentangling Heterogeneous Soil Moisture Patterns in Cosmic-Ray Neutron Sensor Footprints, Hydrology and Earth System Sciences, 25, 6547–6566, https://doi.org/10.5194/hess-25-6547-2021, 2021.

Rentschler, T., Werban, U., Ahner, M., Behrens, T., Gries, P., Scholten, T., Teuber, S., and Schmidt, K.: 3D Mapping of Soil Organic Carbon Content and Soil Moisture with Multiple Geophysical Sensors and Machine Learning, Vadose Zone Journal, 19, e20 062, https://doi.org/10.1002/vzj2.20062, 2020.

Robinson, D., Friedman, S., Thomas, A., Hirmas, D., Sullivan, P., and Nemes, A.: Soil Bulk Density and Porosity Connecting Macro- and Micro-Scales through Geometry., Earth-Science Reviews, 268, 105 173, https://doi.org/10.1016/j.earscirev.2025.105173, 2025.

Romero-Ruiz, A., O'Leary, D., Zhao, D., Wu, Y., and Garré, S.: Preface: Illuminating Soil's Hidden Dimensions, a Decade of Progress and Future Directions in Agrogeophysics Research, SOIL, 11, 1041–1051, https://doi.org/10.5194/soil-11-1041-2025, 2025.

Rossi, M., Manoli, G., Pasetto, D., Deiana, R., Ferraris, S., Strobbia, C., Putti, M., and Cassiani, G.: Coupled Inverse Modeling of a Controlled Irrigation Experiment Using Multiple Hydro-Geophysical Data, Advances in Water Resources, 82, 150–165, https://doi.org/10.1016/j.advwatres.2015.03.008, 2015.

Rubin, Y. and Hubbard, S. S., eds.: Hydrogeophysics, no. v. 50 in Water Science and Technology Library, Springer, Dordrecht [Netherlands] ; New York, ISBN 978-1-4020-3101-4 978-1-4020-3102-1, 2005.

Ruehlmann, J. and Körschens, M.: Calculating the Effect of Soil Organic Matter Concentration on Soil Bulk Density, Soil Science Society of America Journal, 73, 876–885, https://doi.org/10.2136/sssaj2007.0149, 2009.

Sato, T.: Analytical Model for Estimating Terrestrial Cosmic Ray Fluxes Nearly Anytime and Anywhere in the World: Extension of PARMA/EXPACS, PLOS ONE, 10, e0144 679, https://doi.org/10.1371/journal.pone.0144679, 2015.

Sato, T.: Analytical Model for Estimating the Zenith Angle Dependence of Terrestrial Cosmic Ray Fluxes, PLOS ONE, 11, e0160 390, https://doi.org/10.1371/journal.pone.0160390, 2016.

Sato, T. and Niita, K.: Analytical Functions to Predict Cosmic-Ray Neutron Spectra in the Atmosphere, Radiation Research, 166, 544–555, https://doi.org/10.1667/RR0610.1, 2006.

Savitzky, A. and Golay, M. J. E.: Smoothing and Differentiation of Data by Simplified Least Squares Procedures., Analytical Chemistry, 36, 1627–1639, https://doi.org/10.1021/ac60214a047, 1964.

Schattan, P., Köhli, M., Schrön, M., Baroni, G., and Oswald, S. E.: Sensing Area-Average Snow Water Equivalent with Cosmic-Ray Neutrons: The Influence of Fractional Snow Cover, Water Resources Research, 55, 10 796–10 812, https://doi.org/10.1029/2019WR025647, 2019.

https://doi.org/10.5194/egusphere-2026-5633
Preprint. Discussion started: 11 November 2026
© Author(s) 2026. CC BY 4.0 License.



Scheiffele, L. M., Baroni, G., Franz, T. E., Jakobi, J., and Oswald, S. E.: A Profile Shape Correction to Reduce the Vertical Sensitivity of Cosmic-ray Neutron Sensing of Soil Moisture, Vadose Zone Journal, 19, e20 083, https://doi.org/10.1002/vzj2.20083, 2020.

Schrön, M., Zacharias, S., Köhli, M., Weimar, J., and Dietrich, P.: Monitoring Environmental Water with Ground Albedo Neutrons and Correction for Incoming Cosmic Rays with Neutron Monitor Data, in: PoS(ICRC2015)231, vol. 231, Proceeding of Science, The Hague, 2015.

Schrön, M., Köhli, M., Scheiffele, L., Iwema, J., Bogena, H. R., Lv, L., Martini, E., Baroni, G., Rosolem, R., Weimar, J., Mai, J., Cuntz, M., Rebmann, C., Oswald, S. E., Dietrich, P., Schmidt, U., and Zacharias, S.: Improving Calibration and Validation of Cosmic-Ray Neutron Sensors in the Light of Spatial Sensitivity, Hydrology and Earth System Sciences, 21, 5009–5030, https://doi.org/10.5194/hess-21-5009-2017, 2017.

Schrön, M., Rosolem, R., Köhli, M., Piussi, L., Schröter, I., Iwema, J., Kögler, S., Oswald, S. E., Wollschläger, U., Samaniego, L., Dietrich, P., and Zacharias, S.: Cosmic-ray Neutron Rover Surveys of Field Soil Moisture and the Influence of Roads, Water Resources Research, 54, 6441–6459, https://doi.org/10.1029/2017WR021719, 2018.

Schrön, M., Nixdorf, E., Schäfer, D., Jakobi, J., Zengerle, C., Rosolem, R., and Zacharias, S.: CoRNy – A Cosmic-Ray Neutron Processing Toolbox for Python, Tech. rep., https://git.ufz.de/CRNS/cornish_pasdy, 2025.

Shafi, U., Mumtaz, R., García-Nieto, J., Hassan, S. A., Zaidi, S. A. R., and Iqbal, N.: Precision Agriculture Techniques and Practices: From Considerations to Applications, Sensors, 19, 3796, https://doi.org/10.3390/s19173796, 2019.

Tian, Z., Li, Z., Liu, G., Li, B., and Ren, T.: Soil Water Content Determination with Cosmic-Ray Neutron Sensor: Correcting Aboveground Hydrogen Effects with Thermal/Fast Neutron Ratio, Journal of Hydrology, 540, 923–933, https://doi.org/10.1016/j.jhydrol.2016.07.004, 2016.

Tso, C.-H. M., Kuras, O., Wilkinson, P. B., Uhlemann, S., Chambers, J. E., Meldrum, P. I., Graham, J., Sherlock, E. F., and Binley, A.: Improved Characterisation and Modelling of Measurement Errors in Electrical Resistivity Tomography (ERT) Surveys, Journal of Applied Geophysics, 146, 103–119, https://doi.org/10.1016/j.jappgeo.2017.09.009, 2017.

Uhlemann, S., Peruzzo, L., Chou, C., Williams, K. H., Wielandt, S., Wang, C., Falco, N., Wu, Y., Carr, B., Meldrum, P., Chambers, J., and Dafflon, B.: Variations in Bedrock and Vegetation Cover Modulate Subsurface Water Flow Dynamics of a Mountainous Hillslope, Water Resources Research, 60, e2023WR036 137, https://doi.org/10.1029/2023WR036137, 2024.

Van Dijck, S. and Van Asch, T.: Compaction of Loamy Soils Due to Tractor Traffic in Vineyards and Orchards and Its Effect on Infiltration in Southern France, Soil and Tillage Research, 63, 141–153, https://doi.org/10.1016/S0167-1987(01)00237-9, 2002.

Van Rossum, G. and Drake, F. L.: Python 3 Reference Manual, CreateSpace, Scotts Valley, CA, ISBN 1-4414-1269-7, 2009.

Vereecken, H., Binley, A., Cassiani, G., Revil, A., and Titov, K., eds.: Applied Hydrogeophysics, vol. 71 of *NATO Science Series*, Springer Netherlands, Dordrecht, ISBN 978-1-4020-4910-1, https://doi.org/10.1007/978-1-4020-4912-5, 2006.

Vereecken, H., Huisman, J. A., Bogena, H., Vanderborght, J., Vrugt, J. A., and Hopmans, J. W.: On the Value of Soil Moisture Measurements in Vadose Zone Hydrology: A Review, Water Resources Research, 44, 2008WR006 829, https://doi.org/10.1029/2008WR006829, 2008.

Vereecken, H., Schnepf, A., Hopmans, J., Javaux, M., Or, D., Roose, T., Vanderborght, J., Young, M., Amelung, W., Aitkenhead, M., Allison, S., Assouline, S., Baveye, P., Berli, M., Brüggemann, N., Finke, P., Flury, M., Gaiser, T., Govers, G., Ghezzehei, T., Hallett, P., Hendricks Franssen, H., Heppell, J., Horn, R., Huisman, J., Jacques, D., Jonard, F., Kollet, S., Lafolie, F., Lamorski, K., Leitner, D., McBratney, A., Minasny, B., Montzka, C., Nowak, W., Pachepsky, Y., Padarian,

https://doi.org/10.5194/egusphere-2026-5633
Preprint. Discussion started: 11 November 2026
© Author(s) 2026. CC BY 4.0 License.

J., Romano, N., Roth, K., Rothfuss, Y., Rowe, E., Schwen, A., Šimůnek, J., Tiktak, A., Van Dam, J., van der Zee, S., Vogel, H., Vrugt, J., Wöhling, T., and Young, I.: Modeling Soil Processes: Review, Key Challenges, and New Perspectives, Vadose Zone Journal, 15, 0, https://doi.org/10.2136/vzj2015.09.0131, 2016.

Vereecken, H., Amelung, W., Bauke, S. L., Bogena, H., Brüggemann, N., Montzka, C., Vanderborght, J., Bechtold, M., Blöschl, G., Carminati, A., Javaux, M., Konings, A. G., Kusche, J., Neuweiler, I., Or, D., Steele-Dunne, S., Verhoef, A., Young, M., and Zhang, Y.: Soil Hydrology in the Earth System, Nature Reviews Earth & Environment, 3, 573–587, https://doi.org/10.1038/s43017-022-00324-6, 2022.

Von Hebel, C., Reynaert, S., Pauly, K., Janssens, P., Piccard, I., Vanderborght, J., Van Der Kruk, J., Vereecken, H., and Garré, S.: Toward High-resolution Agronomic Soil Information and Management Zones Delineated by Ground-based Electromagnetic Induction and Aerial Drone Data, Vadose Zone Journal, 20, e20 099, https://doi.org/10.1002/vzj2.20099, 2021.

Wang, T.-P., Chen, C.-C., Tong, L.-T., Chang, P.-Y., Chen, Y.-C., Dong, T.-H., Liu, H.-C., Lin, C.-P., Yang, K.-H., Ho, C.-J., and Cheng, S.-N.: Applying FDEM, ERT and GPR at a Site with Soil Contamination: A Case Study, Journal of Applied Geophysics, 121, 21–30, https://doi.org/10.1016/j.jappgeo.2015.07.005, 2015.

Watlet, A., Clément, R., Blanchy, G., Camus, F., Dubois, V., Fargier, Y., Forquet, N., Guyard, H., Imig, A., Quatela, V., and Kaufmann, O.: Latest Developments of OhmPi: Towards Small-Scale ERT Surveys and Monitoring Experiments in the Field, in: NSG2023 29th European Meeting of Environmental and Engineering Geophysics, pp. 1–5, European Association of Geoscientists & Engineers, Edinburgh, United Kingdom, https://doi.org/10.3997/2214-4609.202320205, 2023.

Weimar, J., Köhli, M., Budach, C., and Schmidt, U.: Large-Scale Boron-Lined Neutron Detection Systems as a 3He Alternative for Cosmic Ray Neutron Sensing, Frontiers in Water, 2, 16, https://doi.org/10.3389/frwa.2020.00016, 2020.

Wösten, J., Lilly, A., Nemes, A., and Le Bas, C.: Development and Use of a Database of Hydraulic Properties of European Soils, Geoderma, 90, 169–185, https://doi.org/10.1016/S0016-7061(98)00132-3, 1999.

Yu, L., Gao, W., Shamshiri, R., Tao, S., Ren, Y., Zhang, Y., and Su, G.: Review of Research Progress on Soil Moisture Sensor Technology, International Journal of Agricultural and Biological Engineering, 14, 32–42, https://doi.org/10.25165/j.ijabe.20211404.6404, 2021.

Zhang, Y., Zhang, M., Niu, J., Li, H., Xiao, R., Zheng, H., and Bech, J.: Rock Fragments and Soil Hydrological Processes: Significance and Progress, CATENA, 147, 153–166, https://doi.org/10.1016/j.catena.2016.07.012, 2016.

Zhang, Y., Wu, S., Zhao, W., and Xiao, J.: Mesoscale Soil Moisture Measurements along the Rover Route Using the Mobile Cosmic-Ray Neutron Sensing in the Eastern Tibetan Plateau, Geoderma, 450, 117 046, https://doi.org/10.1016/j.geoderma.2024.117046, 2024.

Zreda, M., Desilets, D., Ferré, T. P. A., and Scott, R. L.: Measuring Soil Moisture Content Non-invasively at Intermediate Spatial Scale Using Cosmic-ray Neutrons, Geophysical Research Letters, 35, 2008GL035 655, https://doi.org/10.1029/2008GL035655, 2008.

Zreda, M., Shuttleworth, W. J., Zeng, X., Zweck, C., Desilets, D., Franz, T., and Rosolem, R.: COSMOS: The COsmic-Ray Soil Moisture Observing System, Hydrology and Earth System Sciences, 16, 4079–4099, https://doi.org/10.5194/hess-16-4079-2012, 2012.